



# Degradation of acetaminophen by activated peroxymonosulfate using Co(OH)<sub>2</sub> hollow microsphere supported titanate nanotubes: Insights into sulfate radical production pathway through CoOH<sup>+</sup> activation

Long Chen<sup>a</sup>, Haodong Ji<sup>a,b</sup>, Juanjuan Qi<sup>a,b</sup>, Taobo Huang<sup>a</sup>, Chong-Chen Wang<sup>c</sup>, Wen Liu<sup>a,b,\*</sup>

<sup>a</sup> The Key Laboratory of Water and Sediment Sciences, Ministry of Education, College of Environmental Sciences and Engineering, Peking University, Beijing 100871, PR China

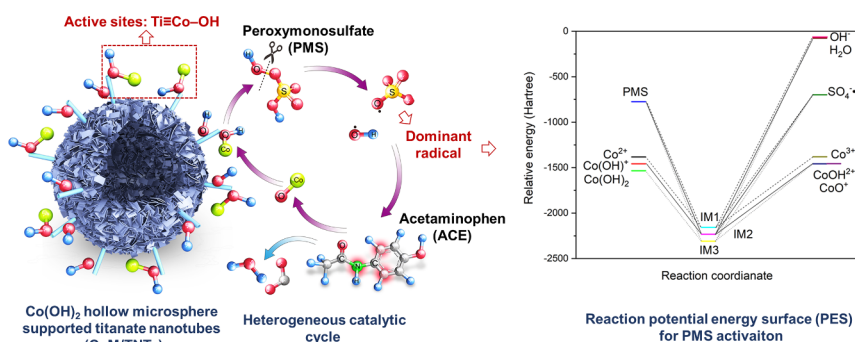
<sup>b</sup> State Environmental Protection Key Laboratory of All Materials Flux in Rivers, College of Environmental Science and Engineering, Peking University, Beijing 100871, PR China

<sup>c</sup> Beijing Key Laboratory of Functional Materials for Building Structure and Environment Remediation, Beijing University of Civil Engineering and Architecture, Beijing 100044, PR China

## HIGHLIGHTS

- CoM/TNTs showed high ACE degradation efficiency after PMS activation.
- Efficient PMS activation was due to the synergic effect of Co(OH)<sub>2</sub> and TNTs.
- TNTs with abundant surface –OH facilitated formation of CoOH<sup>+</sup>.
- PES analysis well explained the higher feasibility of Co(OH)<sup>+</sup> on PMS activation.
- ACE atoms with high Fukui index are active sites for electrophilic attack.

## GRAPHICAL ABSTRACT



## ARTICLE INFO

### Keywords:

Pharmaceuticals  
Sulfate radical  
Titanate  
Heterogeneous catalysis  
DFT calculation

## ABSTRACT

Pharmaceuticals and personal care products (PPCPs) are of great concern due to their increasing health effects, so advanced treatment technologies for PPCPs removal are urgently needed. In this study, titanate nanotubes decorated Co(OH)<sub>2</sub> hollow microsphere (CoM/TNTs) composites were synthesized by a two-step solvothermal method, and used to activate peroxymonosulfate (PMS) through heterogeneous catalysis for acetaminophen (ACE) degradation in water. The optimum material (CoM/TNTs0.5) activated PMS system exhibited high ACE removal efficiency and quick kinetic, as 93.0% ACE was degraded even within 10 min. The two components in CoM/TNTs showed a synergistic effect on PMS activation for radicals production: Co(OH)<sup>+</sup> from CoM was the primary active species to activate PMS, while TNTs could offer abundant –OH groups for Co(OH)<sup>+</sup> formation. Density functional theory (DFT) calculation further interpreted the mechanism of Co(OH)<sup>+</sup> for PMS activation by means of reaction potential energy surface (PES) analysis. Both the scavenger quenching tests and electron paramagnetic resonance analysis revealed that the sulfate radical (SO<sub>4</sub>•<sup>-</sup>) played a dominant role in ACE degradation. Moreover, DFT calculation also suggested that the ACE atoms with high Fukui index (*f*<sup>-</sup>) represented the active sites for electrophilic attack by SO<sub>4</sub>•<sup>-</sup>. The toxicity analysis based on quantitative structure-activity relationship (QSAR) verified the reduced toxicity of transformation products. Furthermore, CoM/TNTs also had

\* Corresponding author at: The Key Laboratory of Water and Sediment Sciences, Ministry of Education, College of Environmental Sciences and Engineering, Peking University, Beijing 100871, PR China.

E-mail address: [wen.liu@pku.edu.cn](mailto:wen.liu@pku.edu.cn) (W. Liu).

<https://doi.org/10.1016/j.cej.2020.126877>

Received 28 April 2020; Received in revised form 28 August 2020; Accepted 29 August 2020

Available online 03 September 2020

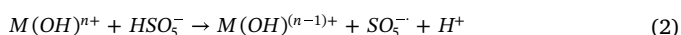
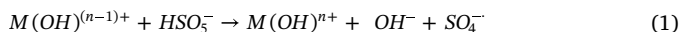
1385-8947/ © 2020 Elsevier B.V. All rights reserved.

good reusability and stability over five cycles. This work provides deep insights into the reaction mechanisms of radical production and organics attack in cobalt-based PMS activation system.

## 1. Introduction

Pharmaceuticals and personal care products (PPCPs) have recently attracted increasing attention due to their potential threats to water environments and human health, including the persistence, hard degradation, biological accumulation and long-term toxicity [1]. Traditional wastewater treatment techniques, such as the activated sludge process, cannot efficiently and steadily remove PPCPs [2,3], so new methods like advanced oxidation processes (AOPs) are urgently needed [4]. Material-enhanced AOPs generally lead to a high yield of reactive oxygen species (ROS) for PPCPs degradation [5,6], and researches in this area focus on key scientific issues including: (1) the efficient generation of radicals in the material-involved heterogeneous system, (2) molecular level interaction mechanisms between radicals and organic pollutants, and (3) deep insights into the degradation pathways of pollutants by means of theoretical calculations.

AOPs such as Fenton reaction, photocatalysis and catalytic ozonation can produce hydroxyl radicals ( $\text{OH}^\cdot$ ,  $E^0 = 1.9\text{--}2.7\text{ V}$ ) to degrade organic pollutants [7,8], including PPCPs [9]. Generally, AOPs show advantages such as a strong oxidation ability, high reaction rate and low disinfection byproducts (DBPs) formation [10]. Recently, AOPs based on the sulfate radical ( $\text{SO}_4^{\cdot-}$ ,  $E^0 = 2.5\text{--}3.1\text{ V}$ ) have attracted significant attention [11].  $\text{SO}_4^{\cdot-}$  acts as an innovative substitute for  $\text{OH}^\cdot$  in the water treatment area, which has a longer half-life time and higher selectivity [12,13].  $\text{SO}_4^{\cdot-}$  is generally generated from peroxymonosulfate (PMS,  $\text{HSO}_5^-$ ) and peroxydisulfate (PDS,  $\text{S}_2\text{O}_8^{2-}$ ) through UV, heat, ultrasound or catalysts [14,15]. In addition, homogenous activation of PMS/PDS by transition metal ions (e.g.,  $\text{Co}^{2+}$ ,  $\text{Fe}^{2+}$ , and  $\text{Ni}^{2+}$ ) is an important method due to the high efficiency [16], but separation of the additional ions from treated water is a big challenge as they may cause secondary pollution [17]. Therefore, heterogeneous activation by transition metals-based catalysts has attracted intensive interests [18], which can achieve restriction of reaction at the interface of material and subsequent easy separation of the catalysts [19]. Transition metal oxides, metal hydroxide, metal-doped materials, bi-metal compounds, modified carbon materials, metal-organic frameworks (MOFs) and their derived materials are all reported to exhibit high PMS activation efficiency to degrade organic contaminants including PPCPs [3,20–27]. Compared with other transition metals such as Fe, Mn and Ni, cobalt-based materials have been identified as the most effective heterogeneous catalysts to activate PMS/PDS [7,11,28]. Moreover, hydroxylated metal species ( $\text{M}(\text{OH})^{(n-1)+}$ ) are widely confirmed as the key form to activate PMS/PDS, and a typical mechanism of transition metal activation process could be summarized as [29,30]:



where M represents transition metal (Cu, Fe, Co, Mn, Ni, etc.). In the process of activation, the metal species can activate PMS to generate sulfate radical by changer transfer, and then form an active cycle to continuously generate reactive species.

The heterogeneous AOPs also suffer from some disadvantages including the catalyst inactivation, the metal ion toxicity and the difficulty in separating the spent catalyst of small size, impeding their field scale application [17]. Therefore, novel materials of high activity, good sedimentation property but less toxicity is of great significance in this area. Previously, transition metals, especially Co(II), have been demonstrated to show a high reactivity for PMS/PDS activation [17]. However, environmental considerations, such as Co leaching, are easy to be ignored. To prevent the leaching of  $\text{Co}^{2+}$  and promote the

catalytic activity, a variety of materials were modified onto cobalt materials, such as molecular sieve SBA-15 [31], carbon-based adsorbent rGO [32], and so on. In recent years, titanate nanotubes (TNTs) have been widely used to modify skeletal materials for catalysis [33]. Therefore, the efficient activation of PMS by TNT- decorated cobalt materials can be expected. First, the large specific surface area (up to  $240.20\text{ m}^2/\text{g}$ ) and hollow tubular structure are beneficial to the stabilization of active sites [34]; second, titanate is an excellent cation adsorbent which can easily adsorb transition metals in the interlayer; and third, the large number of hydroxyl groups ( $-\text{OH}$ ) on TNTs facilitate the formation of  $\text{Co}(\text{OH})^+$  [35], which is confirmed to be the key species for PMS activation [36].

Sulfate radical-based AOPs applied for water treatment have been greatly focused on, and numerous studies have reported heterogenous catalytic activation for  $\text{SO}_4^{\cdot-}$  using functional materials [26,27]. Therefore, the material design strategy is of great significance in this area. Not only a high catalytic activity but also a low toxicity should be considered. Previously, transition metals, especially Co(II), have been demonstrated to show a high reactivity for PMS/PS activation [17]. However, environmental considerations, such as Co leaching, are easy to be ignored. Thus,  $\text{Co}(\text{OH})^+$  (or the  $\equiv\text{Co}-\text{OH}$  complex) has been reported as the most effective species of cobalt for PMS/PS activation [37,38], and this work aims to provide solid theoretical evidence on the effectiveness of hydroxyl cobalt.

In summary, although heterogenous activation of PMS/PDS by cobalt-based materials for environmental cleanup has been widely studied, there are still some scientific challenges: (1) green materials which can efficiently activate PMS/PDS, and can be easily separated from water after practical application need to be developed; (2) the efficiencies of different Co species on PMS activation and the underlying mechanism of radicals production need to be revealed; (3) the electrophilic or nucleophilic properties of radicals on organic contaminant attack need to be illustrated; (4) the reactive sites of specific organic compound, and the degradation pathway in the  $\text{SO}_4^{\cdot-}$ -induced AOP system need to be deeply elucidated by means of both experimental and theoretical methods; and (5) the toxicity evolution of the parent contaminant and its transformation products need to be revealed. Therefore, in this study, a new type of  $\text{Co}(\text{OH})_2$  hollow microsphere decorated with surface-hydroxyl-group-rich titanate nanotubes (CoM/TNTs) composites was developed for PMS activation, and the degradation efficiency of acetaminophen (ACE, a model PPCP) was tested. The degradation mechanism, transformation/degradation pathways, and toxicity evolution of ACE in the CoM/TNTs activated PMS system were systematically studied.

## 2. Materials and methods

### 2.1. Synthesis of CoM/TNTs composites

The chemicals used in this study are listed in [Test S1 of Supplementary data](#), and the physiochemical properties of ACE are presented in [Table S1](#). TNTs were fabricated by a conventional hydrothermal method according to the previous studies [35,39]. To obtain the CoM/TNTs composite materials, alkoxy cobalt microspheres (s-CoA) were synthesized from a solvothermal reaction system firstly ([Fig. S1](#)) [40]. 10 mmol of  $\text{Co}(\text{NO}_3)_2 \cdot 6\text{H}_2\text{O}$  was added into a mixed organic solvent solution (60 mL isopropanol + 16 mL glycerin). After 30 min's stirring to complete dissolution, the solution was transferred into the Teflon in-lined reactor, which was heated at  $180^\circ\text{C}$  for 6 h. The obtained green materials were then washed with ethanol for 3 times and

dried for 12 h at 60 °C. Afterwards, s-CoA (0.5 g) and TNTs in different weights (0.25, 0.5, 1.0 and 2.0 g) were ground, and then dissolved in 80 mL deionized (DI) water and heated at 160 °C for another 3 h, where Co (OH)<sub>2</sub> can form hollow structure with the self-template formation by the Kirkendall effect, grafted with tube structure of TNTs in the surface. After washed with deionized water for 3 times and dried, the final CoM/TNTs products were obtained and labeled as CoM/TNTs2, CoM/TNTs1, CoM/TNTs0.5 and CoM/TNTs0.25 based on the s-CoA and TNTs weight ratio. The pristine Co(OH)<sub>2</sub> was also synthesized by the aforementioned process but without the addition of TNTs.

## 2.2. Material characterization methods

The powder X-ray diffractometer (XRD) analysis was conducted using a D/max-2400 diffractometer (PANalytical, Netherlands) at 40 kV and 100 mA with Cu K $\alpha$  radiation ( $\lambda = 1.542 \text{ \AA}$ ), and a scanning rate of 3.75°/min from 5° to 80° was set. Transmission electron microscopy (TEM) images and energy dispersive spectrometer (EDS) of the materials were recorded on a Tecnai30 FEG (FEI, USA) operated at 300 kV.

The morphological observation of the materials was characterized by a scanning electron microscope (SEM, FEI Quanta 200 FEG, OR, USA). The X-ray photoelectron spectroscopy (XPS) analysis was carried out on an AXIS-Ultra XPS apparatus (Kratos, England) operated at 15 kV and 15 mA with Al K $\alpha$  X-rays as the irradiation source. All the peaks were calibrated by the reference of the standard C 1s peak at a binding energy ( $E_b$ ) of 284.8 eV. The Brunauer-Emmett-Teller (BET) surface area of the sample was obtained on an ASAP 2010 surface area analyzer (Micromeritics, USA) in the relative pressure ( $P/P_0$ ) range of 0.06 – 0.20, while the pore size distribution was obtained following the Barrett-Joyner-Halenda (BJH) method. The nitrogen adsorption at a relative pressure of 0.99 was used to determine the pore volumes and the average pore diameters. The Raman spectra was obtained on a Micro Raman imaging spectrometer (DXRxi, Thermo Fisher Scientific, USA) with an excitation wavelength at 532nm. The zeta potentials and hydrodynamic diameter (size) of the materials at different pH were measured using a Nano-ZS90 Zetasizer (Malvern Instruments, UK). Diffuse reflectance ultraviolet-visible-near infrared (UV-vis-NIR) absorption spectra were obtained on a UV-3600 Plus spectrophotometer

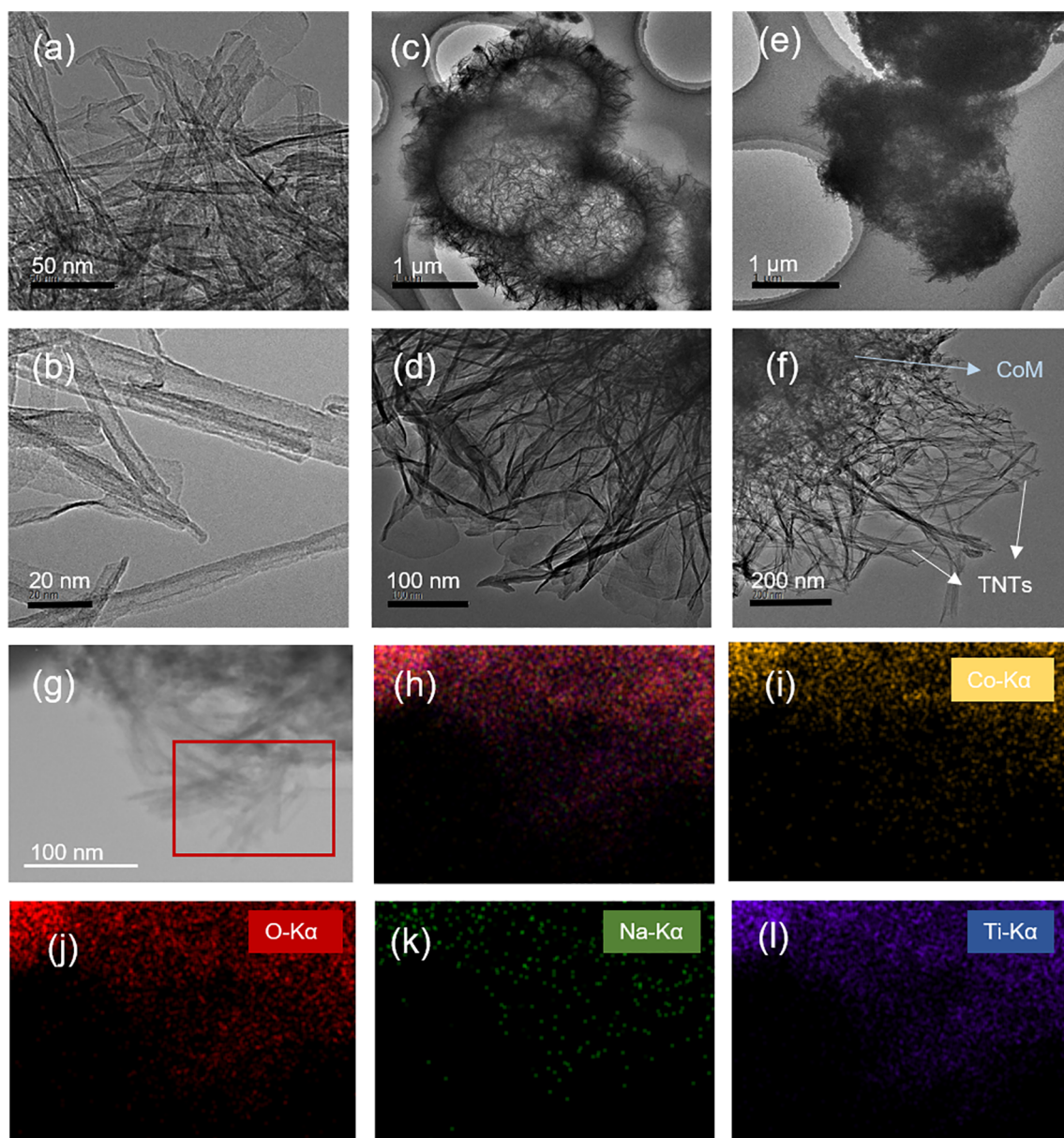


**Fig. 1.** (a, b) TEM images of TNTs, (c, d) Co(OH)<sub>2</sub> hollow microsphere and (e, f) CoM/TNTs0.5; TEM element mapping of (h) all elements, (i) Co, (j) O, (k) Na and (l) Ti for the red square area in CoM/TNTs0.5 (g).



(Shimadzu, Japan), where  $\text{BaSO}_4$  powder was used as the reference at all energies (100% reflectance) and the reflectance measurements were converted to absorption spectra.

### 2.3. Heterogeneous catalysis experiments on ACE degradation

The heterogeneous catalytic degradation experiments were carried out in a 250 mL beaker. In a typical case, 50  $\mu\text{M}$  ACE and 0.2 mM PMS were mixed and magnetically stirred at 400 rpm. Diluted  $\text{HClO}_4$  and NaOH (0.5 mM) were used to adjust the pH to 5. Then, the reaction was proceeded by the addition of 0.1 g/L CoM/TNTs. At predetermined time intervals, each 1 mL sample was taken and filtered through a 0.22  $\mu\text{m}$  nylon filter membrane immediately. The sample vials were pre-filled with 0.1 mL of a 200 mM  $\text{Na}_2\text{SO}_3$  (final concentration of 20 mM, 100 times of PMS dosage) solution to quench the residual radicals. A control test in the absence of any catalysts was carried out, and an experiment on the adsorption of ACE by neat materials without the addition of PMS was also carried out.

To evaluate the contributions of different reactive species to ACE degradation, 50 mM of *tert*-butyl alcohol (TBA) and ethanol were added to quench  $\cdot\text{OH}$  and all radicals, respectively, which is a commonly used method as previously reported [41,42]. The rate constants of TBA with  $\cdot\text{OH}$ , ethanol with  $\cdot\text{OH}$  and ethanol with  $\text{SO}_4^{\cdot-}$  are  $3.8\text{--}7.6 \times 10^8 \text{ M}^{-1} \text{ s}^{-1}$ ,  $1.2\text{--}2.8 \times 10^9 \text{ M}^{-1} \text{ s}^{-1}$  and  $1.6\text{--}7.7 \times 10^7 \text{ M}^{-1} \text{ s}^{-1}$ , respectively [43]. The high rate constant and scavenger concentrations can ensure completely quench the reactions induced by the specific

radicals. To investigate the effect of pH, the solution pH was set to be 3.0–11.0. To test the effects of coexisting cations, 2 mM  $\text{NaNO}_3$ ,  $\text{Ca}(\text{NO}_3)_2$  and  $\text{Fe}(\text{NO}_3)_3$  were added to represent monovalent, divalent and trivalent cations, respectively. To explore the effect of organic matter, humic acid (HA) in concentrations of 1, 5 and 10 mg/L as total organic carbon (TOC) was added. For the experimental procedure on effects of coexisting ions and HA, ACE (50  $\mu\text{M}$ ) was mixed with ions/HA first, and then PMS (0.2 mM) was added. Afterwards, pH of the mixed solution was adjusted to 5.0 using diluted NaOH or  $\text{HClO}_4$ , and finally CoM/TNTs0.5 was added to start the reaction.

ACE was analyzed on an Agilent 1260 II high-performance liquid chromatography (HPLC) system, and the intermediates and transformation products after ACE degradation were captured on an ultrahigh-performance liquid chromatography-mass system (UHPLC, Dionex UltiMate 3000 Series; MS, Thermo Scientific, USA). Total nitrogen and nitrite were analyzed in a flow injection analysis instrument (Skalar San<sup>++</sup>, Netherlands), and ammonia nitrogen was determined by a UV-visible spectrophotometer (UV1800, Shimadzu, Japan). Concentrations of leached Co and Ti ions in solution were analyzed by an inductively coupled plasma-optical emission spectroscopy (ICP-OES, Prodigy, Leeman, USA). Electron paramagnetic resonance (EPR) spectra were obtained on a Bruker EMX/plus X-band EPR spectrometer (Bruker, Billerica, MA).

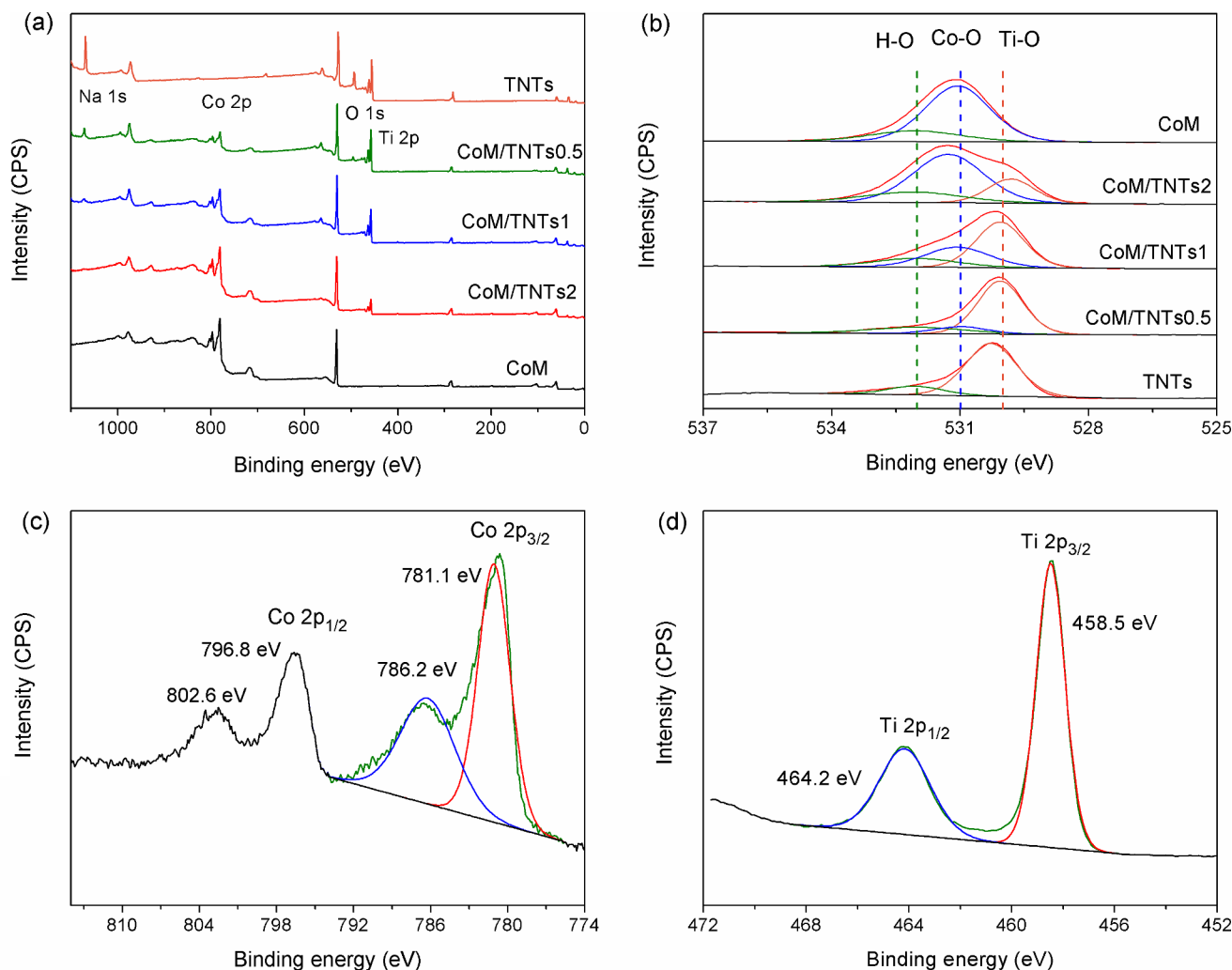


Fig. 2. XPS spectra of TNTs,  $\text{Co}(\text{OH})_2$  and CoM/TNTs composites: (a) Survey spectra; high resolution spectra of (b) O 1s, (c) Co 2p and (d) Ti 2p.

## 2.4. DFT calculations

For the reaction potential energy surface (PES) calculation, the geometry optimizations and vibrational frequencies of reactants, intermediates (IMs), and transformation products (TPs) were all acquired by the B3LYP/6-31 + G\*\* computational methods on Gaussian 16 C.01 software [44]. Then, the detailed energies of all optimized structures were corrected with higher-level single-point energies, i.e., the dispersion-corrected theoretical method B3LYP-D3 (B3LYP with Grimme's DFT-D3 correction) with the standard 6-311 + G\*\* basis set to perform a higher reliability of the energies.

The Fukui function and electrostatic potential (ESP) based on DFT were calculated to predict the regioselectivity of radical attacking the ACE molecule, which were also operated on Gaussian 16 C.01 software [44]. The condensed Fukui index on electrophilic attack was considered in this work [45]:

$$f_A^- = q_{N-1}^A - q_N^A \quad (3)$$

in which  $q^A$  is the atom charge of atom A at the corresponding state, and  $N$  is the charge quantity number. The natural population analysis (NPA) charge was applied to describe the reactive sites.

## 3. Results and discussion

### 3.1. Morphology, crystal phase and composition of CoM/TNTs

TNTs exhibited a tubular nanostructure with an outer diameter of ~9 nm and an inner diameter of ~4.5 nm (Fig. 1a and 1b), which is consistent with our previous reports [46,47]. The synthesized Co(OH)<sub>2</sub> in this study exhibited a hollow microsphere structure with a diameter of 1–1.5 μm (Fig. 1c), and the spherical shell was composed of thin nanosheets (Fig. 1d) [40]. The CoM/TNTs0.5 composite maintained the skeleton structure of the Co(OH)<sub>2</sub> hollow microspheres (Fig. 1e). In the second hydrothermal process for transformation of CoM from precursor s-CoA through hydrolysis, TNTs uniformly grew on the surface of Co(OH)<sub>2</sub> (Fig. 1f), leading to successful compositing of TNTs and Co(OH)<sub>2</sub>. It is noteworthy that Co(OH)<sub>2</sub> can support the growth of TNTs during the second alkaline-hydrothermal process due to the larger size of Co(OH)<sub>2</sub>, resulting in the blooming growth of TNTs. TEM elemental mapping suggests CoM/TNTs0.5 contained Co, O, Ti and Na (Fig. 1g–1l), and all the elements were well dispersed in the material (Fig. 1h). Therefore, TNTs were homogeneously decorated on the shell of Co(OH)<sub>2</sub> microspheres for CoM/TNTs0.5. SEM images also indicated Co(OH)<sub>2</sub> displayed as microspheres with a shell consisting of nanoflakes (Fig. S2a and S2b), while CoM/TNTs0.5 exhibited a spherical structure with TNTs grafted onto the surface (Fig. S2c and 2d).

Fig. S3 shows the XRD patterns of the various materials. In pristine TNTs, the diffractions at  $2\theta = 9.5^\circ, 24.5^\circ, 28.5^\circ$  and  $48.1^\circ$  were assigned to titanate [48,49]. Specifically, the synthesized TNTs are sodium trititanate with a chemical formula of  $H_xNa_{2-x}Ti_3O_7 \cdot nH_2O$  [50], which consists of end-sharing triple [TiO<sub>6</sub>] octahedrons and inter-layered H<sup>+</sup>/Na<sup>+</sup>. For Co(OH)<sub>2</sub> microspheres, the peaks at  $9.5^\circ, 17.8^\circ, 33.7^\circ$  and  $59.5^\circ$  were ascribed to α-Co(OH)<sub>2</sub> [51,52]. The CoM/TNTs nanocomposites exhibited both crystal phases of titanate and α-Co(OH)<sub>2</sub>. In the pattern of CoM/TNTs0.5, the crystal planes of T(102), T(130), T(200) and Co(012) were clearly observed. In addition, the diffraction peaks of T(020) and Co(003) overlapped at  $9.5^\circ$ . The XRD results suggested the successful grafting of TNTs onto Co(OH)<sub>2</sub>. UV-vis-NIR diffuse reflectance spectra also confirmed that the synthesized CoM was α-Co(OH)<sub>2</sub> (Fig. S4), as the strong peaks at 593 and 638 nm were assigned to typical spectroscopic features for α-Co(OH)<sub>2</sub> [53].

Fig. 2 shows the XPS spectra of TNTs, α-Co(OH)<sub>2</sub> and the CoM/TNTs composites, and Table S2 lists the elemental compositions. Co 2p, Na 1s, O 1s and Ti 2p peaks emerged in the CoM/TNTs composite (Fig. 2a). Based on the atomic ratio of the elements and the basic structure of TNTs

( $H_xNa_{2-x}Ti_3O_7 \cdot nH_2O$ ), the synthesized CoM/TNTs0.5, CoM/TNTs1 and CoM/TNTs2 can be expressed as [Co(OH)<sub>2</sub>Na<sub>1.14</sub>H<sub>0.85</sub>Ti<sub>3</sub>O<sub>7</sub>·0.14H<sub>2</sub>O], [Co(OH)<sub>2</sub>0.42Na<sub>0.7</sub>H<sub>1.3</sub>Ti<sub>3</sub>O<sub>7</sub>·0.35H<sub>2</sub>O] and [Co(OH)<sub>2</sub>0.13H<sub>2</sub>Ti<sub>3</sub>O<sub>7</sub>·6.5H<sub>2</sub>O], respectively. The high-resolution XPS spectra of O 1s displayed three oxygen forms (Fig. 2b). In the neat α-Co(OH)<sub>2</sub>, O at 531.1 eV belonged to Co–O [54]; while in the pristine TNTs, O with peaks centered at 530.2 and 532.0 eV were attributed to the lattice oxygen (Ti–O) and surface hydroxyl group (H–O), respectively [35]. With the increase in the Co(OH)<sub>2</sub> fraction in the composite, the proportion of Co–O gradually increased from 11.4% for CoM/TNTs0.5 to 61.5% for CoM/TNTs2. Fig. 2c shows the high-resolution XPS spectrum of Co 2p in CoM/TNTs0.5, and the two peaks at 781.3 (Co 2p<sub>3/2</sub>) and 797.8 eV (Co 2p<sub>1/2</sub>) are in good accordance with the Co(II) in Co(OH)<sub>2</sub> [55]. In addition, the peaks at 786.3 (Co 2p<sub>3/2</sub>) and 802.6 eV (Co 2p<sub>1/2</sub>) were satellite vibrations of Co(II) [51,56]. Fig. 2d shows the Ti 2p XPS spectrum of CoM/TNTs0.5, in which the two broad peaks located at 458.5 and 464.2 eV corresponded to the Ti 2p<sub>3/2</sub> and Ti 2p<sub>1/2</sub> peaks of Ti(IV) [57]. Moreover, in the CoM/TNTs composites, the E<sub>b</sub> of Ti–O shifted to a lower energy while that of Co–O shifted to a lower energy, owing to interaction of CoM with TNTs and electron cloud migration to a positive state after compositing [25]. Therefore, in the CoM/TNTs composite, TNTs with abundant –OH can bond with Co(II), thus, promoting the formation of Co(OH)<sup>+</sup> and the activation of PMS.

Fig. S5a presents the N<sub>2</sub> adsorption-desorption isotherms of Co(OH)<sub>2</sub>, TNTs and CoM/TNTs0.5. All the materials exhibited standard type-IV isotherms, which had a rapid capillary condensation at a relative pressure ( $P/P_0$ ) of 0.45 to 1.0, which is a characteristic of mesoporous structures as defined by International Union of Pure and Applied Chemistry (IUPAC). The existence of mesoporous structure resulted in a large Brunauer-Emmett-Teller (BET) surface area of 132.4 m<sup>2</sup>/g for Co(OH)<sub>2</sub> (Table S3). In addition, TNTs also possessed large BET surface area of 240.2 m<sup>2</sup>/g and pore volume of 1.26 cm<sup>3</sup>/g due to the tubular and hollow nanostructure. CoM/TNTs0.5 showed a larger BET surface area (246.4 m<sup>2</sup>/g) and pore volume (0.67 cm<sup>3</sup>/g). Grafting of TNTs onto CoM maintained the large BET surface area of TNTs, while some pores were blocked due to “penetration” of nanotubes into CoM. Fig. S5b shows that the mesoporous Co(OH)<sub>2</sub> exhibited a pore size distribution centered at ~3.5 nm, assigned to the average voids between nanosheets (Fig. 1d). However, the primary pores of CoM/TNTs0.5 was located at the central peaks of ~3.8 and 8.0 nm, and the peaks at ~8.0 nm belonged to gaps between titanate nanotubes and CoM nanosheets. The larger surface area of CoM/TNTs0.5 facilitated the interface reaction among material, organic molecules and radicals.

### 3.2. Degradation kinetics of ACE and heterogeneous catalytic activation mechanism

Fig. 3 presents the ACE degradation by activated PMS using various materials. PMS could hardly degrade ACE with a low removal efficiency of 4.2% at 10 min [58]. In addition, all the neat materials without the addition of PMS also exhibited low adsorptive removal efficiencies of ACE (< 5%). However, the coexistence of functional materials and PMS led to the efficient removal of ACE, owing to radical production after PMS catalytic activation. Quick ACE degradation kinetics in all the CoM/TNTs activated PMS systems were observed, as a high ACE removal efficiency was obtained only within 10 min. A retarded first-order model was used to describe the reaction longer-term kinetics of ACE degradation [59], where the deviation of reaction rate can be adjusted by incorporating the parameter of “sliding” into the reaction rate constant:

$$C_t = C_0 (1 + \alpha t)^{-k_a/\alpha} \quad (4)$$

where  $C_t$  and  $C_0$  are the real-time and initial concentrations of ACE (mM), respectively;  $t$  is reaction time (min);  $k_a$  is the apparent rate constant (min<sup>−1</sup>), similarly to the initial pseudo-first order rate constant; and  $\alpha$  is the retardation factor expressing the deviation level from the pseudo-first order behavior.

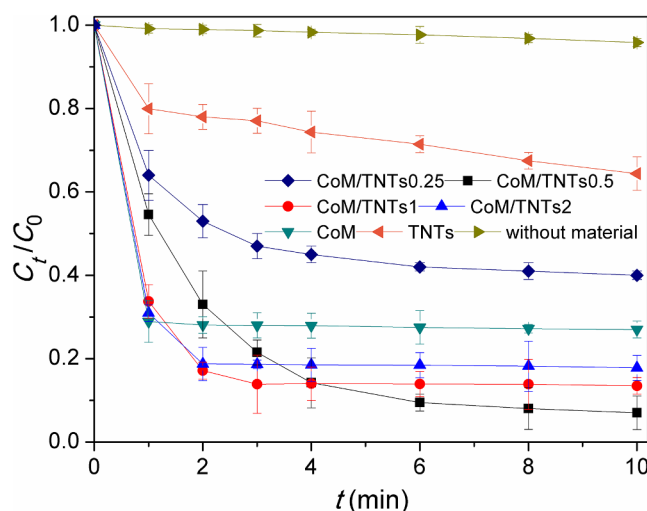


Fig. 3. ACE degradation in various catalytic PMS systems. Experimental conditions: Initial ACE concentration = 50  $\mu\text{M}$ , PMS dosage = 0.2 mM, material dosage = 0.1 g/L, and pH = 5.0.

The degradation efficiency of ACE by neat TNTs activated PMS was 35.6% at 10 min, with a  $k_a$  value of 0.625  $\text{min}^{-1}$  (Table S4). Previous studies have demonstrated that cobalt and its compounds are excellent activating reagents for PMS among the transition metal family [17]. Therefore, the removal efficiency of ACE in  $\text{Co}(\text{OH})_2$  activated PMS system was 73.0%, while ACE was immediately degraded with a high  $k_a$  value of 3.151  $\text{min}^{-1}$ . The degradation of ACE was obviously enhanced in the CoM/TNTs activated PMS systems. Specifically, the ACE removal efficiency at 10 min was 60.3% for CoM/TNTs0.25, 93.0% for CoM/TNTs0.5, 86.5% for CoM/TNTs1 and 79.8% for CoM/TNTs2, respectively. When the proportion of  $\text{Co}(\text{OH})_2$  fraction in the CoM/TNTs composite was very low such as CoM/TNTs0.25, there was not enough Co species to activate PMS, leading to both low  $k_a$  value (1.711  $\text{min}^{-1}$ ) and final ACE removal efficiency (60.3%). When Co content was enough for PMS activation in other three CoM/TNTs composites, a higher proportion of  $\text{Co}(\text{OH})_2$  fraction led to quicker ACE degradation kinetics but to a lower final ACE removal efficiency. Specially, an extremely high  $k_a$  (2.354  $\text{min}^{-1}$ ) was observed for CoM/TNTs2, suggesting very quick reaction kinetics occurred at the start-up stage of reaction; however, the larger retardation factor ( $\alpha=2.534$ ) caused quick attenuation of the rate constant, finally leading to a low ACE removal efficiency of 79.8%. It was different for CoM/TNTs0.5, the reaction was not so dramatic in the early stage with a  $k_a$  value of 0.745  $\text{min}^{-1}$ , and the low retardation factor ( $\alpha=0.382$ ) kept a continuous degradation of ACE, with a final removal efficiency of 93.0%. Thus, CoM/TNTs0.5 was used as the optimum material considering the high final ACE removal efficiency. Great improvement on ACE degradation using CoM/TNTs composites is attributed to the synergetic effect of  $\text{Co}(\text{OH})_2$  and TNTs in the composite. An experiment on PMS activation and ACE degradation by simply mixed  $\text{Co}(\text{OH})_2$  and TNTs was also conducted, and the  $\text{Co}(\text{OH})_2$  to TNTs was set according to the composition of CoM/TNTs0.5 got by XPS. It is found that only 59.4% of ACE was removed at 10 min with a low  $k_a$  value of 1.715  $\text{min}^{-1}$  (Fig. S6). Therefore, synergetic effect of  $\text{Co}(\text{OH})_2$  and TNTs occurred in CoM/TNTs0.5, which is important for efficient PMS activation and ACE degradation. A synergistic factor ( $\Lambda_{\text{syn}}$ , %) based on final ACE removal efficiency is further applied to quantitatively determine the synergy between  $\text{Co}(\text{OH})_2$  and TNTs for ACE degradation, which is modified from the previous reports [60,61]:

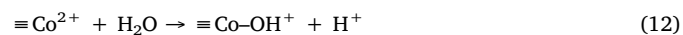
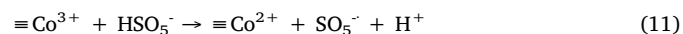
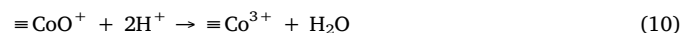
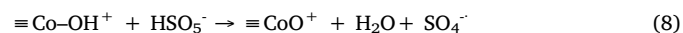
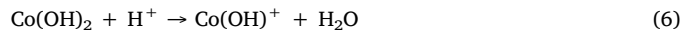
$$\Lambda_{\text{syn}} = \frac{R_{\text{CoM/TNTs0.5}} - (\alpha \times R_{\text{Co}(\text{OH})_2} + \beta \times R_{\text{TNTs}})}{R_{\text{CoM/TNTs0.5}}} \times 100\% \quad (5)$$

where  $R_{\text{CoM/TNTs0.5}}$ ,  $R_{\text{Co}(\text{OH})_2}$  and  $R_{\text{TNTs}}$  are the final ACE removal efficiency by CoM/TNTs0.5,  $\text{Co}(\text{OH})_2$  and TNTs, respectively;  $\alpha$  and  $\beta$

are the weight coefficients for  $\text{Co}(\text{OH})_2$  and TNTs respectively, which are selected to be both 0.5 as CoM/TNTs0.5 presented a chemical formula of  $\text{Co}(\text{OH})_2\text{Na}_{1.14}\text{H}_{0.85}\text{Ti}_3\text{O}_7 \cdot 0.14\text{H}_2\text{O}$  (Table S2).

If the  $\Lambda_{\text{syn}} > 0$ , it means synergistic effect occurs between the two components. The  $\Lambda_{\text{syn}}$  was calculated to be 41.6% ( $> 0$ ) for CoM/TNTs0.5 composite on degradation of ACE, and the high value indicated an obvious synergistic effect between  $\text{Co}(\text{OH})_2$  and TNTs in the CoM/TNTs0.5 composite [60].

The enhanced ACE degradation efficiency in the CoM/TNTs system compared with the neat  $\text{Co}(\text{OH})_2$  system revealed that the TNTs fraction also played an important role in PMS activation, although  $\text{Co}(\text{OH})_2$  was the primary active site [62]. It is widely confirmed that  $\text{Co}(\text{OH})^+$  is the key species to activate PMS [63]. The reactions for PMS activation and ACE degradation included [64]:



where “ $\equiv\text{TiOH}^+$ ” represents TNTs with surface  $-\text{OH}$  groups loaded; “ $\equiv\text{Ti}(\text{OH})\text{Co}^+$ ” and “ $\equiv\text{Co}-\text{OH}^+$ ” represent the material bonded  $\text{Co}(\text{II})$  species (Co linked with  $[\text{Ti}-\text{O}]$ ); “ $\equiv\text{CoO}^+$ ”, “ $\equiv\text{Co}^{3+}$ ” and “ $\equiv\text{Co}^{2+}$ ” are the Co species boned with titanate.

The roles of the TNTs fraction in the composite material for PMS activation can be explained as: (1) TNTs have abundant  $-\text{OH}$  groups on the surface, so a large number of material bonded  $\equiv\text{Co}-\text{OH}$  complexes (linked with  $[\text{Ti}-\text{O}]$ ) will be formed during reaction, leading to efficient PMS activation; (2) TNTs with a good ion-exchange property can retain the formed cobalt cations (e.g.,  $\text{CoO}^+$ ,  $\text{Co}^{3+}$  and  $\text{Co}^{2+}$ ), thus, promoting the Co-induced PMS catalysis cycle (Eqs. (6)–(13)). Dionysiou and his group's research found that application of  $\text{TiO}_2$  as a skeleton to support cobalt-based materials could promote the formation of  $\text{Co}-\text{OH}$  complexes, because surface  $-\text{OH}$  can be easily formed because of the high ability of  $\text{TiO}_2$  to dissociate  $\text{H}_2\text{O}$ . Therefore,  $\text{TiO}_2$ -supported cobalt materials show a high reactivity for PMS activation and organic contaminant degradation [65]. Compared with  $\text{TiO}_2$ , the nanoscale TNTs with abundant  $-\text{OH}$  hybridized with  $\text{Co}(\text{OH})_2$  can greatly promote the formation of  $\text{Co}-\text{OH}$  complexes and the subsequent PMS activation for ACE degradation [66].

To reveal the reaction mechanisms on PMS activation and ACE degradation by CoM/TNTs0.5, the material after reaction was also characterized by means of XRD, TEM, EDS, XPS, Raman, particle size and size distribution, and BET surface area analysis. CoM/TNTs0.5 after reaction displayed similar XRD pattern to that before reaction (Fig. S7), indicating that the crystal phase of the material was well maintained. TEM images indicated that the heterogeneous catalytic reaction did not significantly affect the morphology and size of CoM/TNTs0.5, and the spherical structure with a diameter of  $\sim 2 \mu\text{m}$  still remained (Fig. S8). In addition, the grafted of TNTs on the surface of  $\text{Co}(\text{OH})_2$  were still stable (Fig. S8b and 8d), which showed potential catalytic properties of the material.

The EDS element mapping of CoM/TNTs0.5 depicted that the content of Co decreased after reaction (from 28.5 wt.% to 20.4 wt.%) (Fig. S9), indicating that the active species  $\equiv\text{Co}-\text{OH}$  participated in PMS activation (Eq. (8)) and some of Co released into solution. In addition, XPS spectra also indicated the change of surface elements of CoM/TNTs0.5 after the reaction (Fig. S10). Specifically, the Ti 2p high

resolution spectra showed that the existing forms of Ti did not changed, suggesting the stable  $[\text{TiO}_6]$  octahedrons structure (Fig. S10c). It was consistent with the mechanism that TNTs just acted as skeletal materials to provide  $-\text{OH}$  (Eqs. (7) and (12)). While for the Co 2p high resolution spectra (Fig. S10b), the peak located at 782.6 eV was attributed to the formation of  $\text{Co(II)}-\text{OH}$  complex [67,68], which proved the dominant role of this active species. It was worth noting that the O 1s high resolution spectra changed after reaction (Fig. S10d). O with peak centered at 530.5 eV attributed to Ti-O shifted to the right by 0.3 eV, due to the participation of Ti in the active components  $\text{Ti} \equiv (\text{OH})\text{Co}^+$  (Eq. (7)). The percentage of Co-O increased from 11.47% to 19.22% after reaction, while that of H-O increased from 18.16% to 33.15%, indicating capture of  $\text{Co}^{2+}$  and formation of  $\text{Co}-\text{OH}^+$  on the catalyst surface [69] (Eqs. (7) and (12)). For the Raman spectra of CoM/TNTs0.5 (Fig. S11), the peak at  $276\text{ cm}^{-1}$  was assigned to vibrations involving Ti-O-Na, while the peaks at  $444$  and  $706\text{ cm}^{-1}$  represented

the Ti-O bending vibration in the  $[\text{TiO}_6]$  octahedron, corresponding to titanate nanotube structure [70,71]. The peak at  $535$  and  $1570\text{ cm}^{-1}$  belonged to  $\text{Co(OH)}_2$  [72,73], and the peak at  $845\text{ cm}^{-1}$  was the Ti-O-Co bending vibration formed in the synthesis process. The transformation of Ti-O-Co ( $845\text{ cm}^{-1}$ ) and Co-O ( $1570\text{ cm}^{-1}$ ) after reaction revealed the change of chemical bond, suggesting the success of heterogeneous catalytic reaction.

Fig. S12 shows the hydrodynamic diameter (size) distribution of CoM/TNTs0.5 before and after reaction. The increase of size from 1868 to 2462 nm was attributed to addition of PMS, which increased the ionic strength of the solution and caused aggregation of material [74]. The BET surface area of CoM/TNTs0.5 after reaction decreased from 246.4 to 188.0  $\text{m}^2/\text{g}$  (Fig. S13 and Table S3), which was attributed to: 1) PMS could corrode CoM during heterogeneous catalytic reaction thus leading to block of some pores; 2) adsorption of ACE degraded intermediates resulting in pore filling, and 3) aggradation of the material as

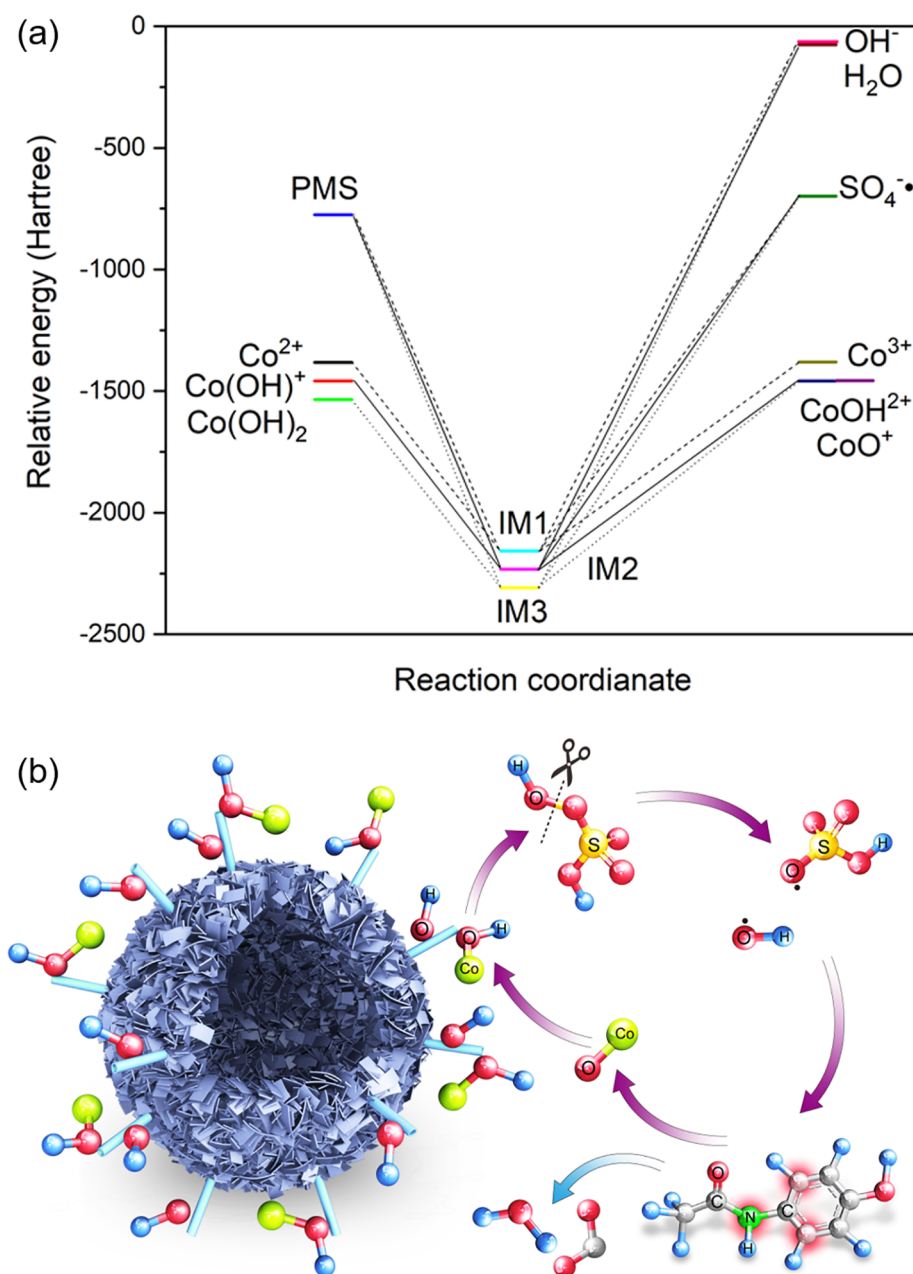


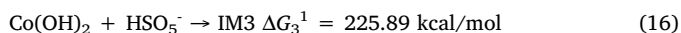
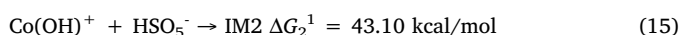
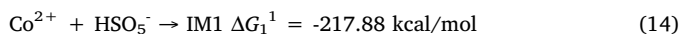
**Fig. 4.** (a) Potential energy surface profiles for the activation process of PMS by various Co(II) species; (b) Schematic diagram of PMS activation and ACE degradation by CoM/TNTs composites.



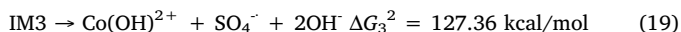
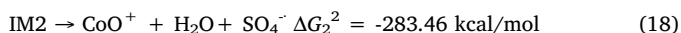
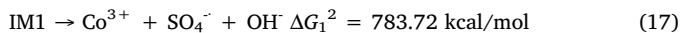
confirmed by hydrodynamic diameter analysis results.

To further confirm hydroxyl cobalt is the most active species for PMS activation, DFT calculations were applied to obtain the activation energies for PMS decomposition by  $\text{Co}(\text{OH})_2$ ,  $\text{Co}(\text{OH})^+$  and  $\text{Co}^{2+}$ . Fig. 4a displays the potential energy surface (PES) profiles for the activation process of PMS by three primary Co(II) species, i.e.,  $\text{Co}^{2+}$ ,  $\text{Co}(\text{OH})^+$  and  $\text{Co}(\text{OH})_2$ . Generally, the PMS activation reactions can be divided into two steps: (I) binding of  $\text{HSO}_5^-$  with the Co(II) species to form IMs (Eqs. (14)–(16)), and (II) IMs cracking into  $\text{SO}_4^{\cdot -}$  and the oxidation products of Co(II) (Eqs. (17)–(19)). It is found that the binding of  $\text{Co}^{2+}$  with  $\text{HSO}_5^-$  is thermodynamically spontaneous with a Gibbs free energy ( $\Delta G_1^1$ ) value of -217.88 kcal/mol. The reaction between  $\text{Co}(\text{OH})^+$  and  $\text{HSO}_5^-$  is also feasible due to the low  $\Delta G_2^1$ , while the binding of  $\text{HSO}_5^-$  with  $\text{Co}(\text{OH})_2$  proceeds with difficulty due to the high  $\Delta G_3^1$  value of 225.89 kcal/mol. In Step II, for sulfate radical formation, cracking IM2 is more feasible due to  $\Delta G_2^2 < 0$ . Although  $\text{Co}^{2+}$  can easily bind with  $\text{HSO}_5^-$ , the subsequent reaction for  $\text{SO}_4^{\cdot -}$  formation is difficult owing to the high  $\Delta G_1^2$  of 783.72 kcal/mol. Therefore, the DFT calculations clearly interpret why  $\text{Co}(\text{OH})^+$  is the most active species of Co(II) for PMS activation.

Step I:



Step II:



The contribution of ROS, mainly including  $\text{SO}_4^{\cdot -}$  and  $\text{OH}^\cdot$ , to ACE degradation in the CoM/TNTs0.5 activated PMS system was evaluated by the scavenger quenching test [75]. TBA is generally employed as a scavenger for  $\text{OH}^\cdot$ , and ethanol is for both  $\text{SO}_4^{\cdot -}$  and  $\text{OH}^\cdot$  [76]. Fig. 5a shows that the addition of TBA almost did not affect ACE degradation, indicating  $\text{OH}^\cdot$  played a negligible role. In comparison, the degradation efficiency of ACE decreased from 93.0% to 36.5% after the addition of ethanol, indicating  $\text{SO}_4^{\cdot -}$  was the dominate ROS. And more than 30% of ACE could be still degraded due to other oxidation mechanisms produced in the reaction system, such as the non-radical oxidation of singlet oxygen ( $^1\text{O}_2$ ) production and electron transferring [77,78],

which was only effective for specific organic pollutants, and more comprehensive demonstration of persulfate oxidation capacity to decompose these pollutants [79]. The EPR analysis further confirmed the production of  $\text{SO}_4^{\cdot -}$  after PMS activation (Fig. 5b). The captured seven distinct peaks without catalyst were assigned to the characteristics of DMPOX by the direct oxidation of PMS [80,81]. While in the presence of catalyst, both the characteristic peaks of  $\text{SO}_4^{\cdot -}$  and  $\text{OH}^\cdot$  were detected, where a four-line spectrum with relative intensities of 1:2:2:1 and hyperfine splitting constant of  $a_N = a_H = 14.9 \text{ G}$  and a six-line signal with the hyperfine splitting constants of DMPO radical adducts in PMS (obtained by simulation,  $a_N = 13.2 \text{ G}$ ,  $a_H = 9.6 \text{ G}$ ,  $a_H = 1.48 \text{ G}$ , and  $a_H = 0.78 \text{ G}$ ) were observed [82,83], suggesting successful PMS activation by CoM/TNTs [84]. Moreover, it is interesting that although  $\text{OH}^\cdot$  was produced, and the PL spectra of terephthalic acid at 425 nm for CoM/TNTs0.5 activated PMS system also confirmed the production of  $\text{OH}^\cdot$  (Fig. S14) [46]; however,  $\text{OH}^\cdot$  did not precipitate in ACE degradation according scavenger quenching results (Fig. 5a), and it is related to the structure and reactive sites of ACE, so  $\text{SO}_4^{\cdot -}$  dominated the ACE degradation in this PMS activation system. Previous studies also reported similar results on the produced  $\text{OH}^\cdot$  played an insignificant role in the degradation of target pollutants in PS/PMS activation system [26,76,85–87]. There are possible two reasons on insignificant role of produced  $\text{OH}^\cdot$ : 1)  $\text{OH}^\cdot$  was produced via the reaction of  $\text{SO}_4^{\cdot -}$  with  $\text{OH}^-$  (Eq. (9),  $k = 6.7 \times 10^7 \text{ M}^{-1} \text{ s}^{-1}$ ) [88]. While for the scavenger quenching test in the presence of ACE,  $\text{SO}_4^{\cdot -}$  preferred to react with ACE first due to the high rate constant ( $1.8 \times 10^9 \text{ M}^{-1} \text{ s}^{-1}$ ) [89], leading to ACE degradation, but not react with  $\text{OH}^-$ . Therefore, although  $\text{OH}^\cdot$  was produced later, but it did not precipitate in ACE degradation and  $\text{SO}_4^{\cdot -}$  played the dominant role. 2) After  $\text{OH}^\cdot$  was produced,  $\text{OH}^\cdot$  was all quenched by TBA due to its high dosage 50 mM, while no residual  $\text{OH}^\cdot$  could attack ACE with low concentration of 50  $\mu\text{M}$ .

Fig. 4b displays the schematic diagram for PMS activation by CoM/TNTs and ACE degradation. As confirmed by the results shown in Fig. S6, the two main components in the CoM/TNTs composite show a synergistic effect: (1) The hollow  $\text{Co}(\text{OH})_2$  microspheres are the Co(II) source, which offer  $\text{Co}^{2+}$  for PMS activation; (2) TNTs can retain the dissolved  $\text{Co}^{2+}$  and then form  $\text{Ti}=\text{OH}\text{Co}^+$  complexes due to the abundant surface hydroxyl groups ( $=\text{TiOH}$ ). Afterwards, PMS is activated by the most active species ( $\text{Co}-\text{OH}$ ) to produce  $\text{SO}_4^{\cdot -}$  and  $\text{OH}^\cdot$  (Eqs. (6)–(9)), and Co(II) is oxidized to Co(III) in the form of  $=\text{CoO}^+$  (Eq. (8)). ACE is gradually degraded and mineralized by the radicals (especially  $\text{SO}_4^{\cdot -}$ ) (Eq. (13)).  $=\text{CoO}^+$  can further be reduced to  $=\text{Co}^{2+}$  by  $\text{HSO}_5^-$  (Eq. (11)). It is a cycle of PMS activation by Co(II), which acts as the key catalytic species. Therefore, synergy of  $\text{Co}(\text{OH})_2$  and TNTs in

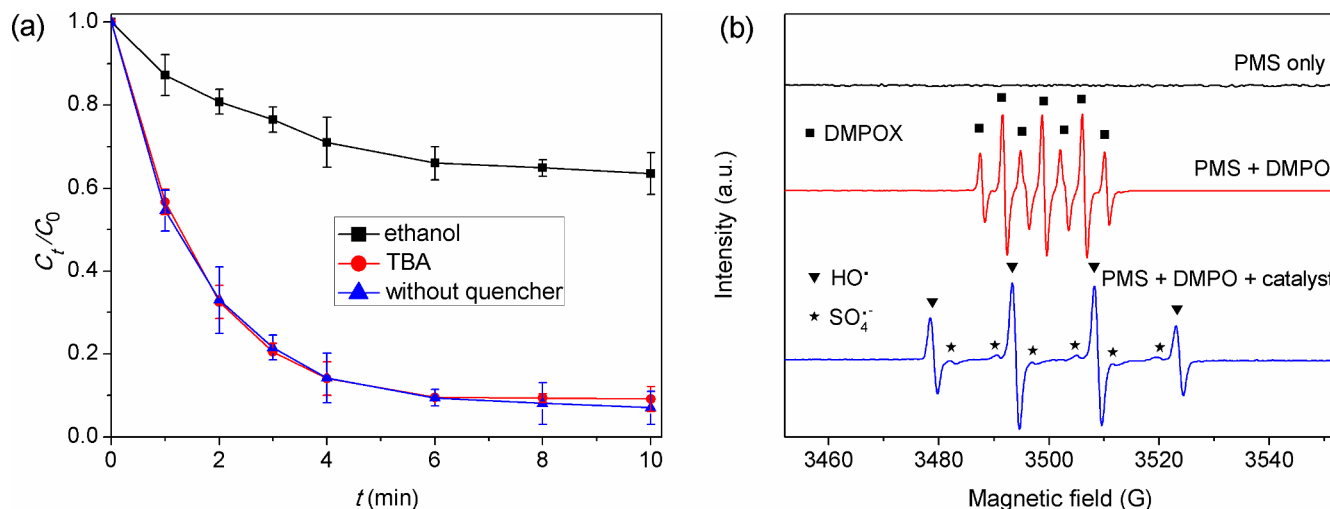


Fig. 5. (a) ACE degradation in the presence of scavengers; (b) EPR spectra at different reaction systems. Experimental conditions: Initial ACE concentration = 50  $\mu\text{M}$ , PMS dosage = 0.2 mM, CoM/TNTs0.5 = 0.1 g/L, TBA or ethanol concentration = 50 mM, pH = 5.0.

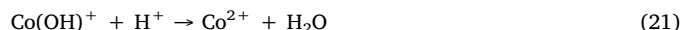


the CoM/TNTs composite not only maintains the Co-activation cycle, but also provides continuous reactive species of  $\text{Co}(\text{OH})^+$ , leading to much higher radicals production and ACE degradation efficiency than the pristine  $\text{Co}(\text{OH})_2$  and TNTs.

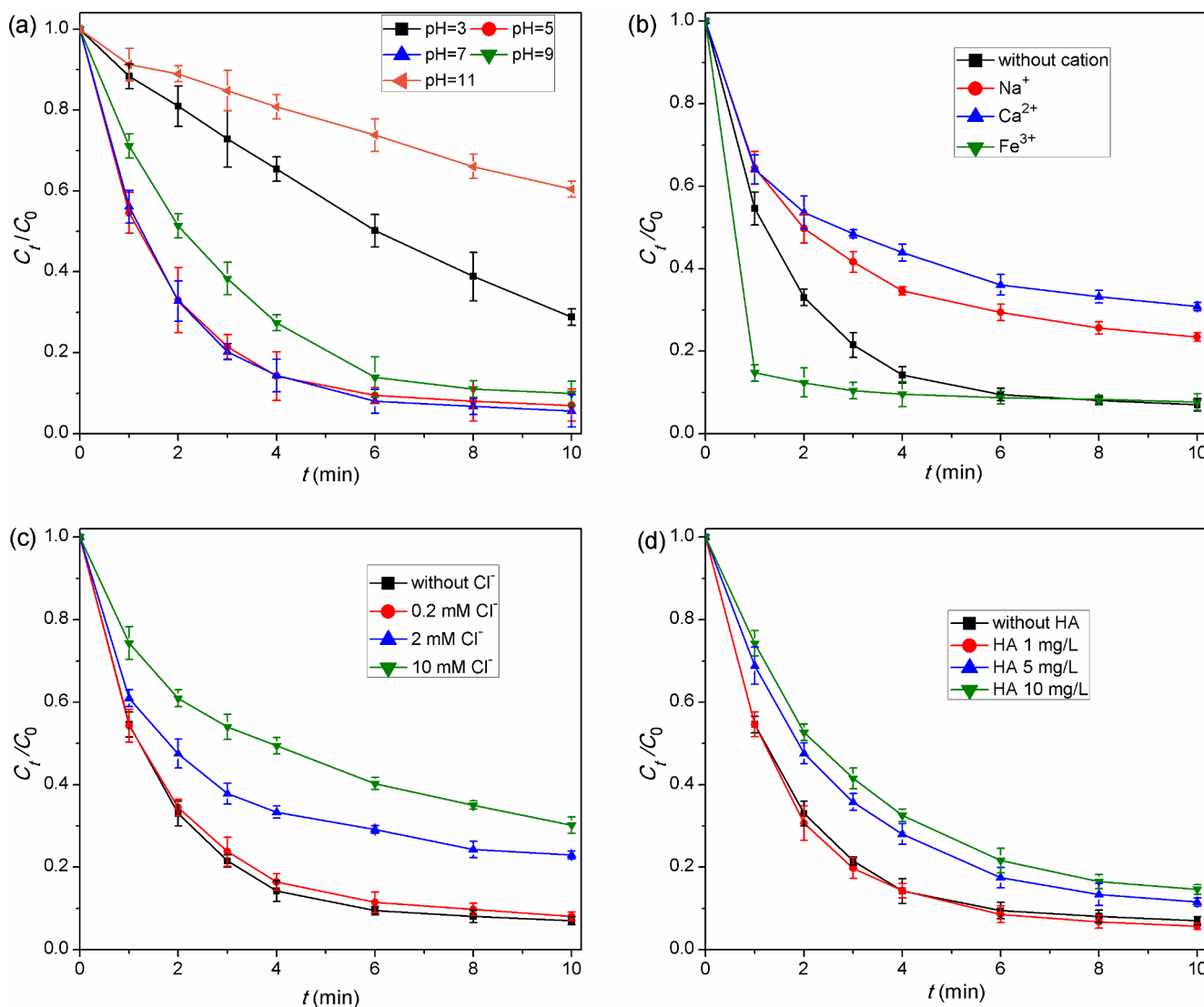
### 3.3. Effects of water chemistry factors

Fig. 6a presents the effect of pH on ACE degradation. High  $k_a$  values were observed at pH 5 ( $0.745 \text{ min}^{-1}$ ) and pH 7 ( $0.685 \text{ min}^{-1}$ ). Both strongly acidic (pH 3) and alkaline (pH 9 and 11) conditions inhibited ACE degradation. pH is highly related to the species of  $\text{Co}(\text{II})$ , thus, affecting PMS activation and radical production. Under strongly alkaline conditions,  $\text{Co}(\text{OH})^+$  tended to form into  $\text{Co}(\text{OH})_2$  (Eq. (20)); in addition,  $\text{SO}_4^{\cdot -}$  also would react with  $\text{OH}^-$  to transform into  $\cdot\text{OH}$  (Eq. (9)), which has a lower oxidation potential under alkaline conditions [17]. Under strongly acidic conditions,  $\text{Co}(\text{OH})^+$  would react with  $\text{H}^+$  to form  $\text{Co}^{2+}$  (Eq. (21)). Both  $\text{Co}(\text{OH})_2$  and  $\text{Co}^{2+}$  were less reactive species for PMS activation. In addition, pH also affected the surface charge of CoM/TNTs0.5 and species of ACE (Fig. S15 and S16). ACE ( $\text{pK}_a = 9.4$ ) mainly existed in the form of an electronegative molecule at  $\text{pH} > 9$ , so the negatively charged material could hardly capture the ACE molecule. Moreover, strongly acidic conditions (pH 3) also caused

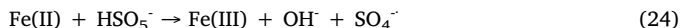
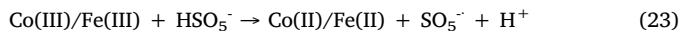
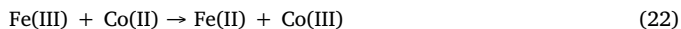
the dissolution of  $\text{Co}(\text{II})$  and the instability of the material.



The addition of  $\text{Na}^+$  and  $\text{Ca}^{2+}$  decreased the ACE removal efficiency from 93.0% to 76.6% and 69.2%, respectively (Fig. 6b). First,  $\text{Na}^+$  and  $\text{Ca}^{2+}$  at high concentrations (2 mM) caused severe material aggregation due to the strong electric double-layer compression effect, thus, inhibiting the interface reaction between PMS and the material. Second,  $\text{Na}^+$  and  $\text{Ca}^{2+}$  would compete for reaction sites with  $\text{Co}^{2+}$ , affecting the binding of  $\text{Co}^{2+}$  to  $-\text{OH}$  on the TNTs' surface. Moreover, the divalent ion ( $\text{Ca}^{2+}$ ) had a stronger double-layer compression effect and ion-exchange ability, so a greater inhibition effect was found than that of monovalent  $\text{Na}^+$  [34]. It is interesting that  $\text{Fe}^{3+}$  obviously enhanced the  $k_a$  value to  $2.567 \text{ min}^{-1}$ , owing to that  $\text{Fe}^{3+}$  can accelerate the cycle of  $\text{Co}(\text{II})/\text{Co}(\text{III})$  and promote the effective conversion of hydroxyl compounds, which might benefit the enhancement of ACE (Eqs. (22) and (23)). Furthermore, the formed  $\text{Fe}(\text{II})$  through the reaction between  $\text{Fe}(\text{III})$  and  $\text{Co}(\text{II})$ , as an excellent transition metal, might also activate PMS to produce  $\text{SO}_4^{\cdot -}$ , and have a synergistic catalytic effect to promote ACE degradation (Eq. (24)) [90,91].



**Fig. 6.** Effects of (a) pH, (b) coexisting cations, (c)  $\text{Cl}^-$  and (d) HA on ACE degradation in the CoM/TNTs0.5 activated PMS system. Experimental conditions: Initial ACE concentration = 50  $\mu\text{M}$ , PMS dosage = 0.2 mM, and CoM/TNTs0.5 = 0.1 g/L; for (a), initial pH was 3.0–11.0; for (b), cation concentration = 2 mM, pH = 5.0; for (c),  $\text{Cl}^-$  = 0.2, 2 and 10 mM, pH = 5.0; and for (d), HA concentration = 1, 5 and 10 mg/L as TOC, pH = 5.0.



A low concentration of 0.2 mM  $\text{Cl}^-$  just slightly inhibited ACE degradation (Fig. 6c). However, the  $k_a$  value dropped from 0.745 to 0.376  $\text{min}^{-1}$  when the  $\text{Cl}^-$  concentration increased from 0 to 10 mM. The inhibition mechanism of  $\text{Cl}^-$  can be explained as: (1)  $\text{Cl}^-$  can directly react with PMS to produce  $\text{HClO}$  and  $\text{Cl}_2$  (Eqs. 25–26), leading to PMS

consumption and less  $\text{SO}_4^{\cdot-}$  production; (2)  $\text{Cl}^-$  is a radical scavenger that can quench  $\text{SO}_4^{\cdot-}$  and form less active substances, such as  $\text{Cl}^\cdot$ ,  $\text{Cl}_2^\cdot$ ,  $\text{Cl}_2$  and  $\text{HClO}$  [92].

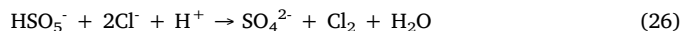


Fig. 6d presents the effect of HA on ACE degradation. At first, 1 mg/L HA had a negligible influence on ACE degradation, while the  $k_a$  value decreased from 0.745 to 0.440 and 0.362  $\text{min}^{-1}$  when the HA

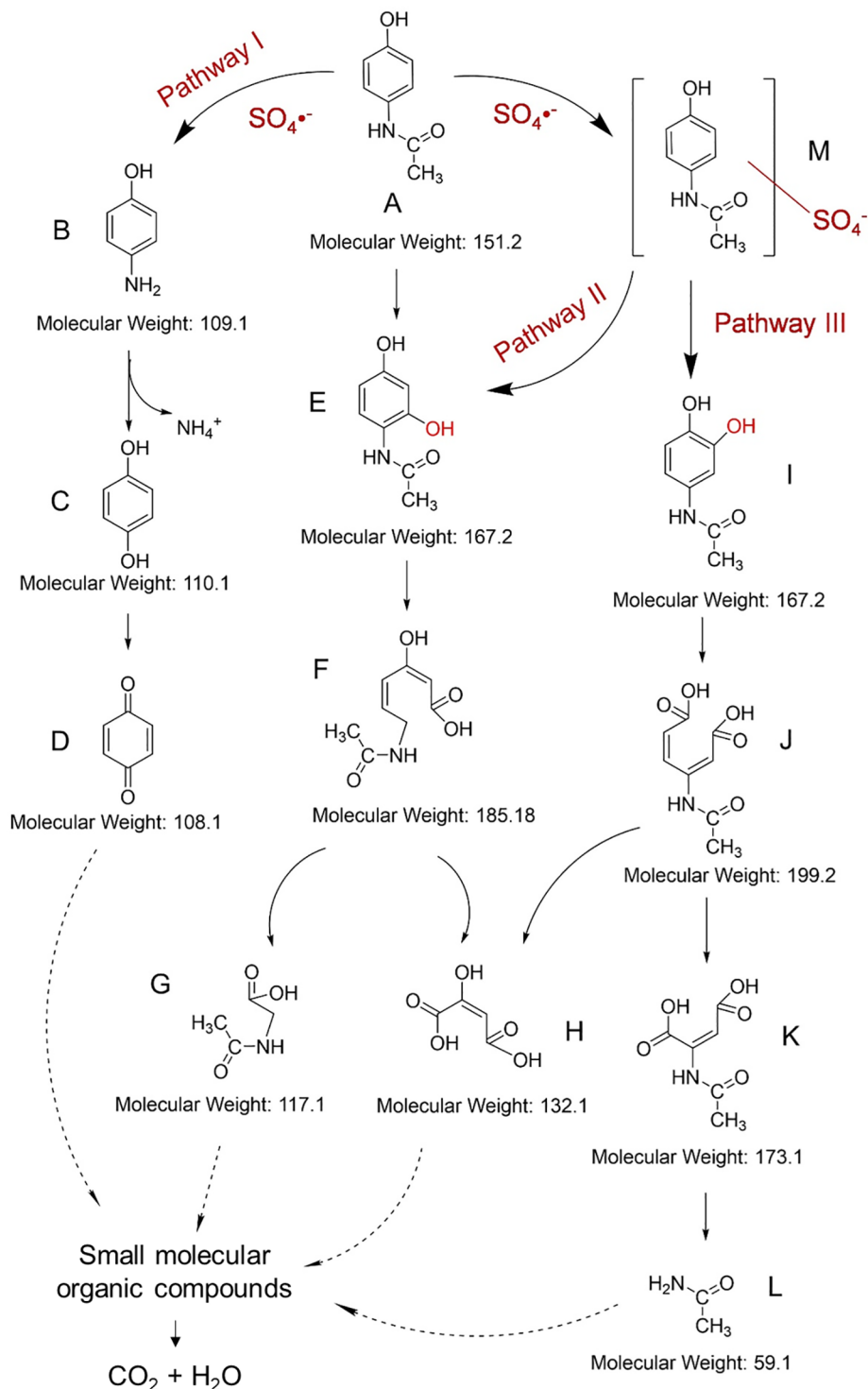


Fig. 7. Proposed degradation pathways of ACE in the CoM/TNTs0.5 activated PMS system.

concentration increased to 5 and 10 mg/L, respectively. The inhibition effect by HA can be attributed to two reasons: Firstly, TNTs can adsorb HA through –OH complexation [34,93], which is also confirmed by the HA adsorption results shown in Fig. S17, and 66.7% of HA ( $C_0 = 10$  mg/L) can be adsorbed onto the material (0.2 g/L) at pH 5. Then, the adsorbed HA will coat onto the surface of the catalyst and prevents mass transfer, especially the interaction between PMS and activating sites. Secondly, HA is widely reported as a radical quenching agent and thus consumes  $SO_4^{\cdot -}$  [94].

### 3.4. Degradation pathway, DFT calculations and toxicity evaluation

To clearly explore the degradation pathway of ACE, the intermediates and products during the oxidation process were detected by LC/MS. Table S5 lists the information on the detected compounds, and Fig. S18 shows the LC/MS chromatograms of degradation intermediates. Fig. 7 depicts the proposed ACE degradation pathway. The elimination of ACE included two main pathways: hydroxylation and cleavage of the C–N bond [95,96]. Generally, the highest occupied molecular orbital (HOMO) represents the ability to lose an electron in a molecule [97], while it cannot quantitatively describe the reactivity of a single atom (Fig. 8c). In recent years, our group has improved the DFT calculation mode based on frontier molecular orbital (FMO) theory and the Fukui index, to accurately describe the electrophilic or nucleophilic reactivity for each site of organic molecule [98,99].

The primary ROS,  $SO_4^{\cdot -}$ , is widely considered as an electrophilic radical [29]. Therefore, DFT calculations were applied to explore the NPA charge distribution and Fukui index representing electrophilic attack ( $f^-$ ) for the ACE molecule (Fig. 8a and 8b). The results indicate that the 15N ( $f^- = 0.1605$ ), 6C ( $f^- = 0.1527$ ), 14O ( $f^- = 0.0863$ ), 2C ( $f^- = 0.0903$ ) and 4C ( $f^- = 0.0860$ ) with higher electrophilic attack Fukui indexes are the most active sites, which are inclined to be attacked by  $SO_4^{\cdot -}$ . However, 14O and 6C are saturated sites that cannot accept radical addition. Therefore, 15N, 2C and 4C are the most

possible sites for  $SO_4^{\cdot -}$  attacking. In addition, the electrostatic potential (ESP) distribution on the ACE molecule surface also suggests the region surrounding 15N prefers to attract the anionic  $SO_4^{\cdot -}$ , thus, promoting the molecular interface reaction (Fig. 8d). Specifically, attacking at 15N leads to the cleavage of the C–N bond (Pathway I: A  $\rightarrow$  B  $\rightarrow$  C  $\rightarrow$  D), while attacking at 4C resulted yields the hydroxylation of ACE (Pathway II: A  $\rightarrow$  M  $\rightarrow$  E  $\rightarrow$  F  $\rightarrow$  G/H and Pathway III: A  $\rightarrow$  M  $\rightarrow$  I  $\rightarrow$  J  $\rightarrow$  H or A  $\rightarrow$  M  $\rightarrow$  I  $\rightarrow$  J  $\rightarrow$  K  $\rightarrow$  L). It is worth noting that the C–N cleavage process was the primary ACE degradation pathway, resulting from the highest 15N Fukui index and the high  $SO_4^{\cdot -}$  contribution. Deep oxidation of ACE by radicals resulted in the mineralization of the small molecular intermediates, i.e., formation of  $CO_2$  and  $H_2O$ . Fig. S19 displays the TOC variation and inorganic nitrogen formation during ACE degradation. It was found that 45.5% of TOC elimination was achieved at 60 min, indicating deep oxidation of ACE in this strong radical-induced system. In addition, 75.7% of organic nitrogen was transformed into  $NH_4^+$ -N, while a low proportion (0.5%) of  $NO_3^-$ -N was formed, which was in good agreement with the primary ACE degradation pathway of C–N cleavage and the emission of  $NH_4^+$  (Pathway I: A  $\rightarrow$  B  $\rightarrow$  C  $\rightarrow$  D in Fig. 7). To achieve complete mineralization of ACE, longer reaction time and larger PMS dosage are needed.

The toxicity of ACE and its degradation intermediates/products were then analyzed by means of the Toxicity Estimation Software Tool (TEST) [99]. The bioaccumulation factor, mutagenicity, *Daphnia magna* LC<sub>50</sub> and oral rat LD<sub>50</sub> were obtained based on the quantitative structure-activity relationship (QSAR) method. Fig. 9a indicates the developed heterogeneous catalytic PMS system can significantly reduce the bioaccumulation factor for most of the intermediates, and only three intermediates (compounds B, C and D) had higher values. For the mutagenicity toxicity (Fig. 9b), ACE was recognized as a mutagenic chemical. After the reaction, the mutagenicity for most of the intermediates was reduced to “mutagenicity negative”. ACE with a *Daphnia magna* LC<sub>50</sub> value of 38.11 mg/L was considered “harmful”, while several intermediates/products turned to “nontoxic” (Fig. 9c).

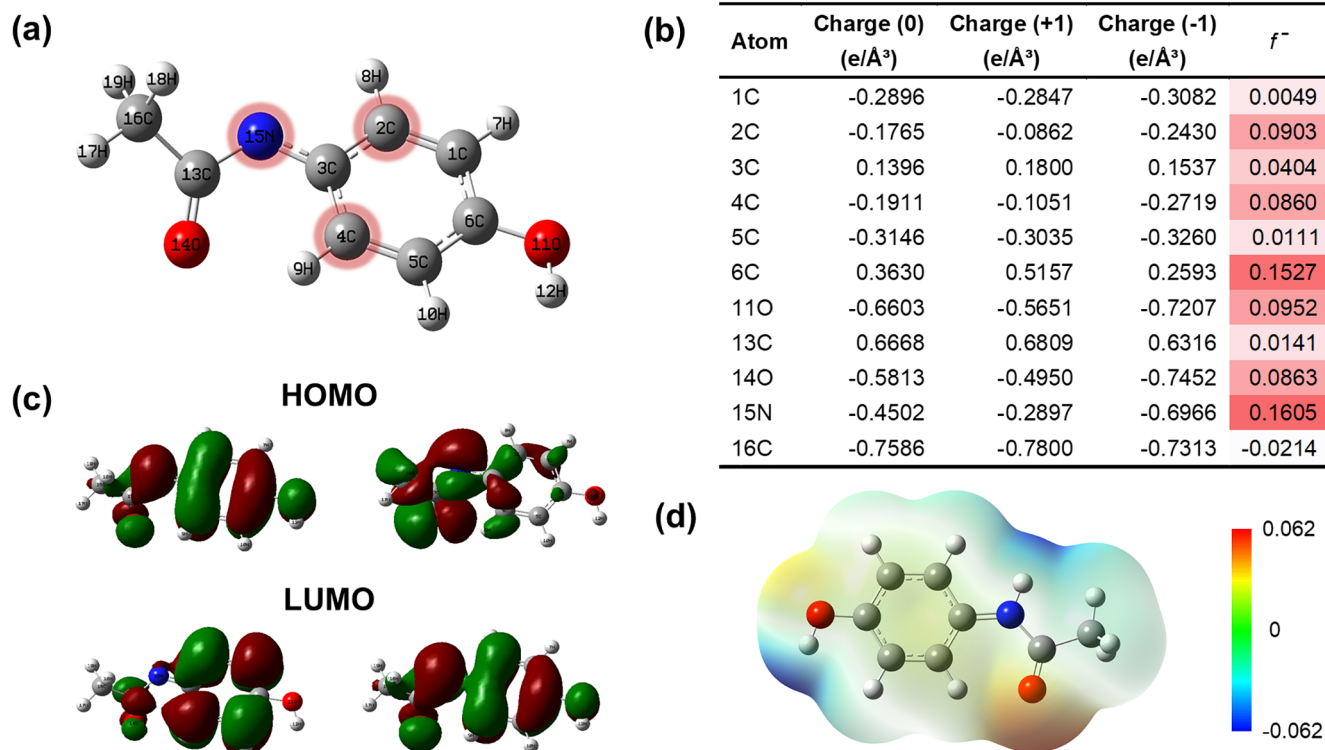


Fig. 8. Natural bond orbital (NBO) analysis for the ACE molecule at B3LYP/6-31 + G(d) level. (a) ACE molecule structure; (b) Natural population analysis (NPA) charge populations and condensed Fukui index distribution for electrophilic attack ( $f^-$ ); (c) The highest occupied molecular orbital (HOMO) and the lowest unoccupied molecular orbital (LUMO); (d) Electrostatic potential (ESP)-mapped molecular surface of ACE.



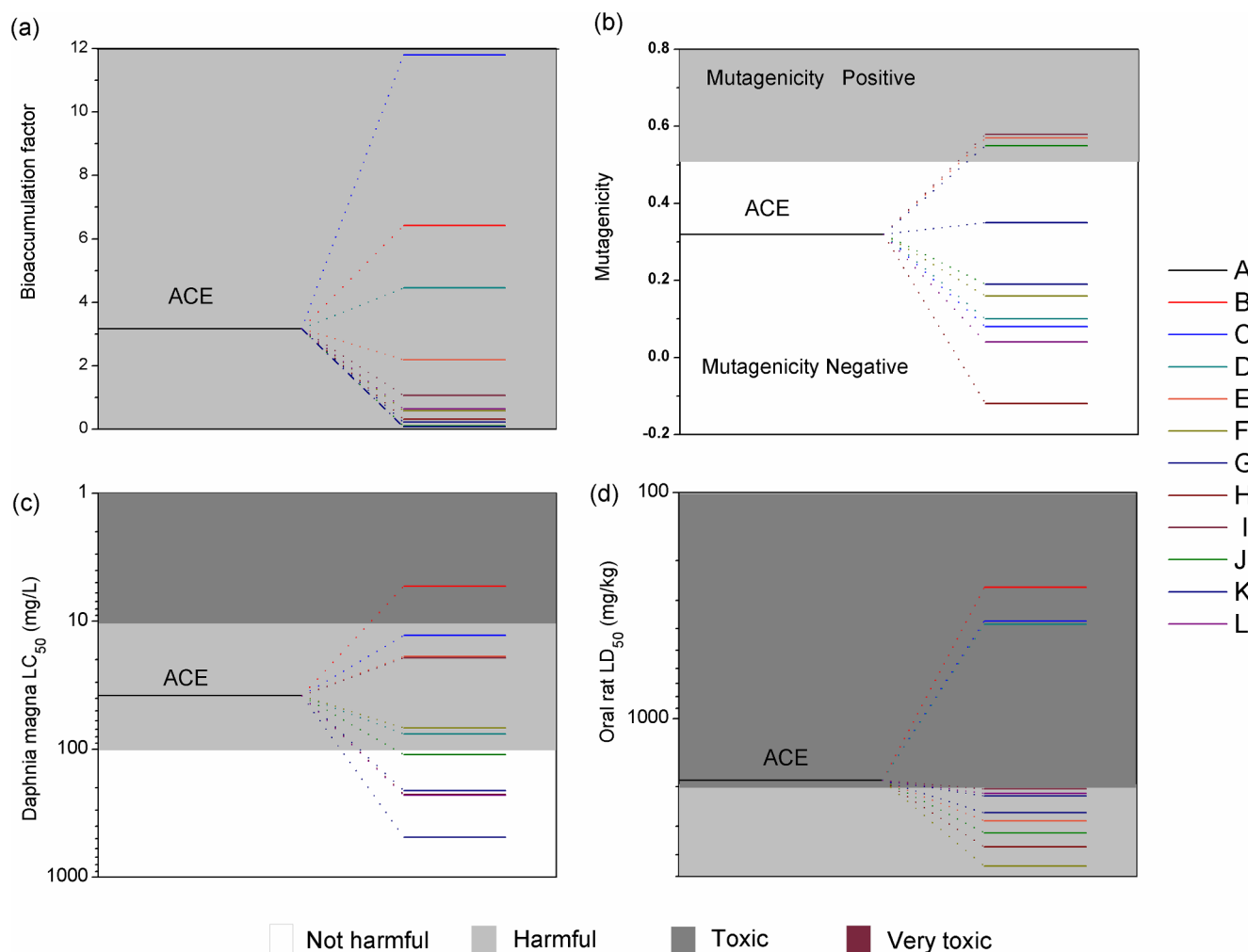


Fig. 9. Theoretical calculated (a) bioaccumulation factor, (b) mutagenicity, (c) *Daphnia magna* LC<sub>50</sub> and (d) oral rat LD<sub>50</sub> of ACE and degradation intermediates.

Similarly, the oral rat LD<sub>50</sub> of ACE is 1875 mg/kg, which belonged to the “toxic” level (Fig. 9d). After degradation, almost all the intermediates/products showed higher LD<sub>50</sub> values and thus reduced acute toxicity. Therefore, the proposed catalytic PMS process is a “green” technology for organic degradation because of the general toxicity attenuation effect. It is also worth noting that some of the intermediates exhibited a higher toxicity, so deep oxidation or complete minimization is recommended.

### 3.5. Reusability and stability of CoM/TNTs0.5 and perspective of the activated PMS for water treatment

Fig. S20 presents the degradation of ACE via the CoM/TNTs0.5 activated PMS over five reuse cycles (Reuse methods shown in Text S4). Even in the 5th cycle, > 90% of ACE was degraded, indicating the good reusability of CoM/TNTs0.5 for PMS activation. In addition, limited Co dissolution (20.4%) was observed after five cycles, while as high as 64.8% of Co(II) was leached into solution when using neat Co(OH)<sub>2</sub> as a catalyst. The reason for the high stability of CoM/TNTs0.5 was attributed to the TNT component in the composite, as TNTs could retain the Co(II) cations due to the good adsorptive performance and excellent ion-exchange property [34].

Table S6 compares degradation efficiency of ACE in different AOP systems. It was clear that the proposed CoM/TNTs0.5-induced PMS activation system was more efficient for ACE removal considering the low material (0.1 g/L) and PMS (0.2 mM) dosage. In addition, very quick ACE removal kinetics was obtained just within 10 min, which is

important for practical application and energy conservation. Moreover, retention of Co ions in the materials also reduced the secondary pollution potential by the leached metal ions. The efficiency of heterogeneous catalytic system was also evaluated on degradation of other typical pollutants, including methyl orange (MO), phenol, sulfa-chloropyridazine (SCP), ciprofloxacin (CIP) and sulfamethazine (SMT) (Fig. S21). It is found that 89.5% of SCP, 85.6% of SMT, 84.9% of CIP, 63.5% of MO and 66.5% of phenol could be degraded in 10 min, so the proposed technique showed a good degradation capacity for a wide range of organic contaminants. Therefore, CoM/TNTs composites showed high practical application potential for wastewater treatment. In the future, degradation of PPCPs in the real wastewater with complicated water chemistry parameters is expected to be conducted, and the respective roles of released cobalt ions and material bonded Co species in PMS activation also need to be further explored.

## 4. Conclusions

This study developed a new class of Co(OH)<sub>2</sub> hollow microsphere supported titanate nanotubes composites to activate PMS, and achieved the goal of efficient ACE degradation. CoM/TNTs exhibited a structure of TNTs homogenously coating onto the Co(OH)<sub>2</sub> hollow microsphere, and the formed Ti–O–Co played a key role in PMS activation. In the presence of PMS, CoM/TNTs composites showed enhanced ACE degradation efficiency compared with the neat TNTs and Co(OH)<sub>2</sub>. The optimum catalyst CoM/TNTs0.5 could quickly degrade 93.0% of ACE with only 0.1 g/L of material and 0.2 mM of PMS at pH 5.0. The two

main components in the CoM/TNTs composite have a synergetic effect on PMS activation: theoretical calculations demonstrate that  $\text{CoOH}^+$  is the most active species for PMS activation while TNTs can offer abundant  $-\text{OH}$  groups for Co-OH complexes formation.  $\text{SO}_4^{\cdot-}$  was the key ROS for ACE degradation. DFT calculations combined with LC/MS analysis revealed that ACE degradation pathway was driven by the cleavage of C-N bond and hydroxylation, and 15N was the most active site. Toxicological simulation also indicated that the oxidation system was beneficial to organics toxicity reducing.

In the future, for material development for PMS/PDS activation, supporting materials rich with  $-\text{OH}$  are recommended to be applied as the skeleton. Furthermore, DFT calculations on the Fukui index can describe the reactive sites of organic contaminants well; therefore, it is a powerful tool to deeply investigate the contaminant degradation pathway and should be used for transformation product control if available.

### Declaration of Competing Interest

The authors declare that they have no known competing financial interests or personal relationships that could have appeared to influence the work reported in this paper.

### Acknowledgements

Financial support from the National Natural Science Foundation of China (NSFC) (No. 21906001, No. 51539001 and No. 51721006) and China Postdoctoral Science Foundation (No. 2019M650007) is greatly acknowledged. This work is also supported by the Beijing Nova Program (Z19111000110000).

### Appendix A. Supplementary data

Supplementary data to this article can be found online at <https://doi.org/10.1016/j.cej.2020.126877>.

### References

- [1] K. Guo, Z. Wu, C. Shang, B. Yao, S. Hou, X. Yang, W. Song, J. Fang, Radical chemistry and structural relationships of PPCP degradation by UV/chlorine treatment in simulated drinking water, *Environ. Sci. Technol.* 51 (2017) 10431–10439.
- [2] J. Kim, T. Zhang, W. Liu, P. Du, J.T. Dobson, C.H. Huang, Advanced oxidation process with peracetic acid and Fe(II) for contaminant degradation, *Environ. Sci. Technol.* 53 (2019) 13312–13322.
- [3] T. Zhang, Y. Chen, T. Leiknes, Oxidation of refractory benzothiazoles with PMS/ $\text{CuFe}_2\text{O}_4$ : Kinetics and transformation intermediates, *Environ. Sci. Technol.* 50 (2016) 5864–5873.
- [4] Z. Cai, A.D. Dwivedi, W.-N. Lee, X. Zhao, W. Liu, M. Sillanpää, D. Zhao, C.-H. Huang, J. Fu, Application of nanotechnologies for removing pharmaceutically active compounds from water: development and future trends, *Environ. Sci. Nano* 5 (2018) 27–47.
- [5] J. Lim, Y. Yang, M.R. Hoffmann, Activation of peroxymonosulfate by oxygen vacancies-enriched cobalt-doped black  $\text{TiO}_2$  nanotubes for the removal of organic pollutants, *Environ. Sci. Technol.* 53 (2019) 6972–6980.
- [6] Y. Wu, F. Wang, X. Jin, X. Zheng, Y. Wang, D. Wei, Q. Zhang, Y. Feng, Z. Xie, P. Chen, H. Liu, G. Liu, Highly active metal-free carbon dots/g- $\text{C}_3\text{N}_4$  hollow porous nanospheres for solar-light-driven PPCPs remediation: Mechanism insights, kinetics and effects of natural water matrices, *Water Res.* 172 (2020) 115492.
- [7] P. Hu, M. Long, Cobalt-catalyzed sulfate radical-based advanced oxidation: A review on heterogeneous catalysts and applications, *Appl. Catal. B: Environ.* 181 (2016) 103–117.
- [8] J. Wang, R. Zhuan, Degradation of antibiotics by advanced oxidation processes: An overview, *Sci. Total Environ.* 701 (2020) 135023.
- [9] M.E. Sillanpää, T.A. Kurniawan, W.H. Lo, Degradation of chelating agents in aqueous solution using advanced oxidation process (AOP), *Chemosphere* 83 (2011) 1443–1460.
- [10] I.A. Ike, T. Karanfil, J. Cho, J. Hur, Oxidation byproducts from the degradation of dissolved organic matter by advanced oxidation processes - A critical review, *Water Res.* 164 (2019) 114929.
- [11] W.D. Oh, Z.L. Dong, T.T. Lim, Generation of sulfate radical through heterogeneous catalysis for organic contaminants removal: Current development, challenges and prospects, *Appl. Catal. B: Environ.* 194 (2016) 169–201.
- [12] R. Luo, C. Liu, J. Li, C. Wang, X. Sun, J. Shen, W. Han, L. Wang, Convenient synthesis and engineering of ultrafine  $\text{Co}_3\text{O}_4$ -incorporated carbon composite: towards practical application of environmental remediation, *J. Mater. Chem. A* 6 (2018) 3454–3461.
- [13] H. Li, C. Shan, B. Pan, Fe(III)-doped g- $\text{C}_3\text{N}_4$  mediated peroxymonosulfate activation for selective degradation of phenolic compounds via high-valent iron-oxo species, *Environ. Sci. Technol.* 52 (2018) 2197–2205.
- [14] R. Dewil, D. Mantzavinos, I. Poullos, M.A. Rodrigo, New perspectives for advanced oxidation processes, *J. Environ. Manage.* 195 (2017) 93–99.
- [15] J. Lee, U. von Gunten, J.H. Kim, Persulfate-based advanced oxidation: Critical assessment of opportunities and roadblocks, *Environ. Sci. Technol.* 54 (2020) 3064–3081.
- [16] S. Wacławek, H.V. Lutze, K. Gröbel, V.V.T. Padil, M. Černík, D.D. Dionysiou, Chemistry of persulfates in water and wastewater treatment: A review, *Chem. Eng. J.* 330 (2017) 44–62.
- [17] J. Wang, S. Wang, Activation of persulfate (PS) and peroxymonosulfate (PMS) and application for the degradation of emerging contaminants, *Chem. Eng. J.* 334 (2018) 1502–1517.
- [18] Y. Lei, C.S. Chen, Y.J. Tu, Y.H. Huang, H. Zhang, Heterogeneous degradation of organic pollutants by persulfate activated by  $\text{CuO-Fe}_3\text{O}_4$ : Mechanism, stability, and effects of pH and bicarbonate ions, *Environ. Sci. Technol.* 49 (2015) 6838–6845.
- [19] B. Betti, S.H. Sonawane, B.A. Bhanvase, S.P. Gumfekar, Nanomaterials-based advanced oxidation processes for wastewater treatment: A review, *Chem. Eng. Process.* 109 (2016) 178–189.
- [20] L. Wang, H. Xu, N. Jiang, Z. Wang, J. Jiang, T. Zhang, Trace cupric species triggered decomposition of peroxymonosulfate and degradation of organic pollutants: Cu(III) being the primary and selective intermediate oxidant, *Environ. Sci. Technol.* 54 (2020) 4686–4694.
- [21] Y. Gao, Y. Zhu, L. Lyu, Q. Zeng, X. Xing, C. Hu, Electronic structure modulation of graphitic carbon nitride by oxygen doping for enhanced catalytic degradation of organic pollutants through peroxymonosulfate activation, *Environ. Sci. Technol.* 52 (2018) 14371–14380.
- [22] Z. Wu, Y. Wang, Z. Xiong, Z. Ao, S. Pu, G. Yao, B. Lai, Core-shell magnetic  $\text{Fe}_3\text{O}_4@ \text{Zn/Co-ZIFs}$  to activate peroxymonosulfate for highly efficient degradation of carbamazepine, *Appl. Catal. B: Environ.* 277 (2020) 119136.
- [23] S. Wang, J. Tian, Q. Wang, F. Xiao, S. Gao, W. Shi, F. Cui, Development of  $\text{CuO}$  coated ceramic hollow fiber membrane for peroxymonosulfate activation: a highly efficient singlet oxygen-dominated oxidation process for bisphenol A degradation, *Appl. Catal. B: Environ.* 256 (2019) 117783.
- [24] J. Jiang, X. Wang, C. Zhang, T. Li, Y. Lin, T. Xie, S. Dong, Porous  $\text{OD/3D NiCo}_2\text{O}_4/\text{g-C}_3\text{N}_4$  accelerate emerging pollutant degradation in PMS/vis system: Degradation mechanism, pathway and toxicity assessment, *Chem. Eng. J.* 397 (2020) 125356.
- [25] X. Tao, P. Pan, T. Huang, L. Chen, H. Ji, J. Qi, F. Sun, W. Liu, In-situ construction of  $\text{Co(OH)}_2$  nanoparticles decorated urchin-like  $\text{WO}_3$  for highly efficient degradation of sulfachloropyridazine via peroxymonosulfate activation: Intermediates and DFT calculation, *Chem. Eng. J.* 395 (2020) 125186.
- [26] Z. Wang, W. Qiu, S. Pang, Y. Gao, Y. Zhou, Y. Cao, J. Jiang, Relative contribution of ferryl ion species ( $\text{Fe(IV)}$ ) and sulfate radical formed in nanoscale zero valent iron activated peroxydisulfate and peroxymonosulfate processes, *Water Res.* 172 (2020) 115504.
- [27] D. Xia, Y. Li, G. Huang, R. Yin, T. An, G. Li, H. Zhao, A. Lu, P.K. Wong, Activation of persulfates by natural magnetic pyrrhotite for water disinfection: Efficiency, mechanisms, and stability, *Water Res.* 112 (2017) 236–247.
- [28] G.P. Anipsitakis, D.D. Dionysiou, Degradation of organic contaminants in water with sulfate radicals generated by the conjunction of peroxymonosulfate with cobalt, *Environ. Sci. Technol.* 37 (2003) 4790–4797.
- [29] R. Xiao, Z. Luo, Z. Wei, S. Luo, R. Spinney, W. Yang, D.D. Dionysiou, Activation of peroxymonosulfate/persulfate by nanomaterials for sulfate radical-based advanced oxidation technologies, *Curr. Opin. Chem. Eng.* 19 (2018) 51–58.
- [30] X. Duan, C. Su, J. Miao, Y. Zhong, Z. Shao, S. Wang, H. Sun, Insights into perovskite-catalyzed peroxymonosulfate activation: Maneuverable cobalt sites for promoted evolution of sulfate radicals, *Appl. Catal. B: Environ.* 220 (2018) 626–634.
- [31] C. Cai, S. Kang, X. Xie, C. Liao, Ultrasound-assisted heterogeneous peroxymonosulfate activation with Co/SBA-15 for the efficient degradation of organic contaminant in water, *J. Hazard. Mater.* 385 (2020) 121519.
- [32] L.G. Devi, M. Srinivas, Hydrothermal synthesis of reduced graphene oxide- $\text{CoFe}_2\text{O}_4$  heteroarchitecture for high visible light photocatalytic activity: Exploration of efficiency, stability and mechanistic pathways, *J. Environ. Chem. Eng.* 5 (2017) 3243–3255.
- [33] X. Liu, P. Du, W. Pan, C. Dang, T. Qian, H. Liu, W. Liu, D. Zhao, Immobilization of uranium (VI) by niobate/titanate nanoflakes heterojunction through combined adsorption and solar-light-driven photocatalytic reduction, *Appl. Catal. B: Environ.* 231 (2018) 11–22.
- [34] T. Wang, W. Liu, L. Xiong, N. Xu, J.R. Ni, Influence of pH, ionic strength and humic acid on competitive adsorption of Pb(II), Cd(II) and Cr(III) onto titanate nanotubes, *Chem. Eng. J.* 215 (2013) 366–374.
- [35] W. Liu, T. Wang, A.G.L. Borthwick, Y.Q. Wang, X.C. Yin, X.Z. Li, J.R. Ni, Adsorption of  $\text{Pb}^{2+}$ ,  $\text{Cd}^{2+}$ ,  $\text{Cu}^{2+}$  and  $\text{Cr}^{3+}$  onto titanate nanotubes: Competition and effect of inorganic ions, *Sci. Total Environ.* 456 (2013) 171–180.
- [36] K.H. Chan, W. Chu, Degradation of atrazine by cobalt-mediated activation of peroxymonosulfate: Different cobalt counteranions in homogenous process and cobalt oxide catalysts in photolytic heterogeneous process, *Water Res.* 43 (2009) 2513–2521.
- [37] P. Shi, X. Dai, H. Zheng, D. Li, W. Yao, C. Hu, Synergistic catalysis of  $\text{Co}_3\text{O}_4$  and graphene oxide on  $\text{Co}_3\text{O}_4/\text{GO}$  catalysts for degradation of Orange II in water by advanced oxidation technology based on sulfate radicals, *Chem. Eng. J.* 240 (2014) 264–270.
- [38] Q. Yang, H. Choi, D.D. Dionysiou, Nanocrystalline cobalt oxide immobilized on

- titanium dioxide nanoparticles for the heterogeneous activation of peroxymonosulfate, *Appl. Catal. B: Environ.* 74 (2007) 170–178.
- [39] W. Liu, J. Ni, X. Yin, Synergy of photocatalysis and adsorption for simultaneous removal of Cr(VI) and Cr(III) with TiO<sub>2</sub> and titanate nanotubes, *Water Res.* 53 (2014) 12–25.
- [40] J. Zhao, Y.C. Zou, X.X. Zou, T.Y. Bai, Y.P. Liu, R.Q. Gao, D.J. Wang, G.D. Li, Self-template construction of hollow Co<sub>3</sub>O<sub>4</sub> microspheres from porous ultrathin nanosheets and efficient noble metal-free water oxidation catalysts, *Nanoscale* 6 (2014) 7255–7262.
- [41] J.-C.-E. Yang, Y. Lin, H.-H. Peng, B. Yuan, D.D. Dionysiou, X.-D. Huang, D.-D. Zhang, M.-L. Fu, Novel magnetic rod-like Mn-Fe oxycarbide toward peroxymonosulfate activation for efficient oxidation of butyl paraben: Radical oxidation versus singlet oxygenation, *Appl. Catal. B: Environ.* 268 (2020) 118549.
- [42] X. Dong, B. Ren, X. Zhang, X. Liu, Z. Sun, C. Li, Y. Tan, S. Yang, S. Zheng, D.D. Dionysiou, Diatomite supported hierarchical 2D CoNi<sub>3</sub>O<sub>4</sub> nanoribbons as highly efficient peroxymonosulfate catalyst for atrazine degradation, *Appl. Catal. B: Environ.* 272 (2020) 118971.
- [43] C. Zhu, F. Zhu, D.D. Dionysiou, D. Zhou, G. Fang, J. Gao, Contribution of alcohol radicals to contaminant degradation in quenching studies of persulfate activation process, *Water Res.* 139 (2018) 66–73.
- [44] M. Frisch, G. Trucks, H. Schlegel, G. Scuseria, M. Robb, J. Cheeseman, G. Scalmani, V. Barone, G. Petersson, H. Nakatsuji, Gaussian 16, Revision A 3 (2016).
- [45] R.G. Parr, W. Yang, Density functional approach to the frontier-orbital theory of chemical reactivity, *J. Am. Chem. Soc.* 106 (1984) 4049–4050.
- [46] X. Zhao, Z. Cai, T. Wang, S.E. O'Reilly, W. Liu, D. Zhao, A new type of cobalt-deposited titanate nanotubes for enhanced photocatalytic degradation of phenanthrene, *Appl. Catal. B: Environ.* 187 (2016) 134–143.
- [47] J. Ma, F. Li, T. Qian, H. Liu, W. Liu, D. Zhao, Natural organic matter resistant powder activated charcoal supported titanate nanotubes for adsorption of Pb(II), *Chem. Eng. J.* 315 (2017) 191–200.
- [48] N. Li, L. Zhang, Y. Chen, M. Fang, J. Zhang, H. Wang, Highly efficient, irreversible and selective ion exchange property of layered titanate nanostructures, *Adv. Funct. Mater.* 22 (2012) 835–841.
- [49] K. Cheng, Z. Cai, J. Fu, X. Sun, W. Sun, L. Chen, D. Zhang, W. Liu, Synergistic adsorption of Cu(II) and photocatalytic degradation of phenanthrene by a jaboticaba-like TiO<sub>2</sub>/titanate nanotube composite: An experimental and theoretical study, *Chem. Eng. J.* 358 (2019) 1155–1165.
- [50] X. Li, W. Liu, J. Ni, Short-cut synthesis of tri-titanate nanotubes using nano-anatase: Mechanism and application as an excellent adsorbent, *Microporous Mesoporous Mater.* 213 (2015) 40–47.
- [51] H. Jin, S. Mao, G. Zhan, F. Xu, X. Bao, Y. Wang, Fe incorporated  $\alpha$ -Co(OH)<sub>2</sub> nanosheets with remarkably improved activity towards the oxygen evolution reaction, *J. Mater. Chem. A* 5 (2017) 1078–1084.
- [52] T. Deng, W. Zhang, O. Arcelus, J.G. Kim, J. Carrasco, S.J. Yoo, W. Zheng, J. Wang, H. Tian, H. Zhang, X. Cui, T. Rojo, Atomic-level energy storage mechanism of cobalt hydroxide electrode for pseudocapacitors, *Nat. Commun.* 8 (2017) 15194.
- [53] S. Kalasina, P. Pattanasattayavong, M. Sukomboon, N. Phattharasupakun, J. Wuthiprom, M. Sawangphruk, A new concept of charging supercapacitors based on the photovoltaic effect, *Chem. Commun. (Camb)* 53 (2017) 709–712.
- [54] T. Xue, X. Wang, J.-M. Lee, Dual-template synthesis of Co(OH)<sub>2</sub> with mesoporous nanowire structure and its application in supercapacitor, *J. Power Sources* 201 (2012) 382–386.
- [55] G. Nie, J. Huang, X. Wang, Layered Co(OH)<sub>2</sub> deposited polymeric carbon nitrides for photocatalytic water oxidation, *ACS Catal.* 5 (2015) 941–947.
- [56] M. Cheng, G. Zeng, D. Huang, C. Lai, Y. Liu, C. Zhang, J. Wan, L. Hu, C. Zhou, W. Xiong, Efficient degradation of sulfamethazine in simulated and real wastewater at slightly basic pH values using Co-SAM-SCS /H<sub>2</sub>O<sub>2</sub> Fenton-like system, *Water Res.* 138 (2018) 7–18.
- [57] W. Liu, Z. Cai, X. Zhao, T. Wang, F. Li, D. Zhao, High-capacity and photoregenerable composite material for efficient adsorption and degradation of phenanthrene in water, *Environ. Sci. Technol.* 50 (2016) 11174–11183.
- [58] C. Tan, N. Gao, Y. Deng, J. Deng, S. Zhou, J. Li, X. Xin, Radical induced degradation of acetaminophen with Fe<sub>3</sub>O<sub>4</sub> magnetic nanoparticles as heterogeneous activator of peroxymonosulfate, *J. Hazard. Mater.* 276 (2014) 452–460.
- [59] B. Han, M. Zhang, D. Zhao, Y. Feng, Degradation of aqueous and soil-sorbed estradiol using a new class of stabilized manganese oxide nanoparticles, *Water Res.* 70 (2015) 288–299.
- [60] G. Nie, J. Huang, Y. Hu, Y. Ding, X. Han, H. Tang, Heterogeneous catalytic activation of peroxymonosulfate for efficient degradation of organic pollutants by magnetic Cu<sup>0</sup>/Fe<sub>3</sub>O<sub>4</sub> submicron composites, *Chin. J. Catal.* 38 (2017) 227–239.
- [61] R.R. Solis, F.J. Rivas, O. Gimeno, J.L. Pérez-Bote, Photocatalytic ozonation of clopyralid, picloram and triclopyr. Kinetics, toxicity and influence of operational parameters, *J. Chem. Technol. Biot.* 91 (2016) 51–58.
- [62] M.F. Ma, L. Chen, J.Z. Zhao, W. Liu, H.D. Ji, Efficient activation of peroxymonosulfate by hollow cobalt hydroxide for degradation of ibuprofen and theoretical study, *Chin. Chem. Lett.* 30 (2019) 2191–2195.
- [63] L. Wu, Y. Yu, Q. Zhang, J. Hong, J. Wang, Y. She, A novel magnetic heterogeneous catalyst oxygen-defective CoFe<sub>2</sub>O<sub>4-x</sub> for activating peroxymonosulfate, *Appl. Surf. Sci.* 480 (2019) 717–726.
- [64] Y. Huang, Z. Wang, Q. Liu, X. Wang, Z. Yuan, J. Liu, Effects of chloride on PMS-based pollutant degradation: A substantial discrepancy between dyes and their common decomposition intermediate (phthalic acid), *Chemosphere* 187 (2017) 338–346.
- [65] H. Choi, E. Stathatos, D.D. Dionysiou, Sol-gel preparation of mesoporous photocatalytic TiO<sub>2</sub> films and TiO<sub>2</sub>/Al<sub>2</sub>O<sub>3</sub> composite membranes for environmental applications, *Appl. Catal. B: Environ.* 63 (2006) 60–67.
- [66] P. Du, J. Chang, H. Zhao, W. Liu, C. Dang, M. Tong, J. Ni, B. Zhang, Sea-buckthorn-like MnO<sub>2</sub> decorated titanate nanotubes with oxidation property and photocatalytic activity for enhanced degradation of 17 $\beta$ -estradiol under solar light, *ACS Appl. Energy Mater.* 1 (2018) 2123–2133.
- [67] A. Khan, Z. Liao, Y. Liu, A. Jawad, J. Iftikhar, Z. Chen, Synergistic degradation of phenols using peroxymonosulfate activated by CuO-Co<sub>3</sub>O<sub>4</sub>/MnO<sub>2</sub> nanocatalyst, *J. Hazard. Mater.* 329 (2017) 262–271.
- [68] Q. Yang, H. Choi, S.R. Al-Abed, D.D. Dionysiou, Iron-cobalt mixed oxide nanocatalysts: Heterogeneous peroxymonosulfate activation, cobalt leaching, and ferromagnetic properties for environmental applications, *Appl. Catal. B: Environ.* 88 (2009) 462–469.
- [69] Y. Ren, L. Lin, J. Ma, J. Yang, J. Feng, Z. Fan, Sulfate radicals induced from peroxymonosulfate by magnetic ferrosin MF<sub>2</sub>O<sub>4</sub> (M = Co, Cu, Mn, and Zn) as heterogeneous catalysts in the water, *Appl. Catal. B: Environ.* 165 (2015) 572–578.
- [70] D. Nepak, D. Srinivas, Spectroscopy and catalytic activity study of gold supported on barium titanate nanotubes for styrene epoxidation, *Appl. Catal. A: Gen.* 523 (2016) 61–72.
- [71] W. Liu, X. Zhao, T. Wang, D. Zhao, J. Ni, Adsorption of U(VI) by multilayer titanate nanotubes: Effects of inorganic cations, carbonate and natural organic matter, *Chem. Eng. J.* 286 (2016) 427–435.
- [72] D. Khallafallah Hassen, M.M. Selim, S.A. El-Safty, K.A. Khalil, G. Abu el-Maged, M. Dewidar, Graphene-supported Co(OH)<sub>2</sub> mesostructures for ethanol oxidation reaction electrocatalysis, *Nano-Struct. Nano-Obj.* 9 (2017) 31–39.
- [73] J. Yang, H. Liu, W.N. Martens, R.L. Frost, Synthesis and characterization of cobalt hydroxide, cobalt oxyhydroxide, and cobalt oxide nanodiscs, *J. Phys. Chem. C* 114 (2010) 111–119.
- [74] G.O. Martins, M. Segalla Petrónio, A.M. Furuyama Lima, A.M. Martinez Junior, V.A. de Oliveira Tiera, M. de Freitas Calmon, P.S. Leite Vilamaior, S.W. Han, M.J. Tiera, Amphiphilic chitosan improves the physicochemical properties of siRNA-chitosan nanoparticles at physiological conditions, *Carbohydr. Polym.* 216 (2019) 332–342.
- [75] Y. Du, W. Ma, P. Liu, B. Zou, J. Ma, Magnetic CoFe<sub>2</sub>O<sub>4</sub> nanoparticles supported on titanate nanotubes (CoFe<sub>2</sub>O<sub>4</sub>/TNTs) as a novel heterogeneous catalyst for peroxymonosulfate activation and degradation of organic pollutants, *J. Hazard. Mater.* 308 (2016) 58–66.
- [76] T. Zeng, X. Zhang, S. Wang, H. Niu, Y. Cai, Spatial confinement of a Co<sub>3</sub>O<sub>4</sub> catalyst in hollow metal-organic frameworks as a nanoreactor for improved degradation of organic pollutants, *Environ. Sci. Technol.* 49 (2015) 2350–2357.
- [77] Y. Gao, Z. Chen, Y. Zhu, T. Li, C. Hu, New insights into the generation of singlet oxygen in the metal-free peroxymonosulfate activation process: Important role of electron-deficient carbon atoms, *Environ. Sci. Technol.* 54 (2020) 1232–1241.
- [78] R. Luo, M. Li, C. Wang, M. Zhang, M.A. Nasir Khan, X. Sun, J. Shen, W. Han, L. Wang, J. Li, Singlet oxygen-dominated non-radical oxidation process for efficient degradation of bisphenol A under high salinity condition, *Water Res.* 148 (2019) 416–424.
- [79] H. Xu, N. Jiang, D. Wang, L. Wang, Y. Song, Z. Chen, J. Ma, T. Zhang, Improving PMS oxidation of organic pollutants by single cobalt atom catalyst through hybrid radical and non-radical pathways, *Appl. Catal. B: Environ.* 263 (2020) 118350.
- [80] K.Z. Huang, H. Zhang, Direct electron-transfer-based peroxymonosulfate activation by iron-doped manganese oxide ( $\delta$ -MnO<sub>2</sub>) and the development of galvanic oxidation processes (GOPs), *Environ. Sci. Technol.* 53 (2019) 12610–12620.
- [81] C. Li, Y. Huang, X. Dong, Z. Sun, X. Duan, B. Ren, S. Zheng, D.D. Dionysiou, Highly efficient activation of peroxymonosulfate by natural negatively-charged kaolinite with abundant hydroxyl groups for the degradation of atrazine, *Appl. Catal. B: Environ.* 247 (2019) 10–23.
- [82] Y. Zhao, H. An, J. Feng, Y. Ren, J. Ma, Impact of crystal types of AgFeO<sub>2</sub> nanoparticles on the peroxymonosulfate activation in the water, *Environ. Sci. Technol.* 53 (2019) 4500–4510.
- [83] Y. Zhou, X. Wang, C. Zhu, D.D. Dionysiou, G. Zhao, G. Fang, D. Zhou, New insight into the mechanism of peroxymonosulfate activation by sulfur-containing minerals: Role of sulfur conversion in sulfate radical generation, *Water Res.* 142 (2018) 208–216.
- [84] H. Zhang, C. Li, L. Lyu, C. Hu, Surface oxygen vacancy inducing peroxymonosulfate activation through electron donation of pollutants over cobalt-zinc ferrite for water purification, *Appl. Catal. B: Environ.* 270 (2020) 118874.
- [85] B. Sun, W. Ma, N. Wang, P. Xu, L. Zhang, B. Wang, H. Zhao, K.-Y.A. Lin, Y. Du, Polyaniline: A new metal-free catalyst for peroxymonosulfate activation with highly efficient and durable removal of organic pollutants, *Environ. Sci. Technol.* 53 (2019) 9771–9780.
- [86] Y. Zhang, J. Zhou, X. Chen, L. Wang, W. Cai, Coupling of heterogeneous advanced oxidation processes and photocatalysis in efficient degradation of tetracycline hydrochloride by Fe-based MOFs: Synergistic effect and degradation pathway, *Chem. Eng. J.* 369 (2019) 745–757.
- [87] S.B. Hammouda, F. Zhao, Z. Safaei, D.L. Ramasamy, B. Doshi, M. Sillanpää, Sulfate radical-mediated degradation and mineralization of bisphenol F in neutral medium by the novel magnetic Sr<sub>2</sub>CoFeO<sub>6</sub> double perovskite oxide catalyzed peroxymonosulfate: Influence of co-existing chemicals and UV irradiation, *Appl. Catal. B: Environ.* 233 (2018) 99–111.
- [88] Y. Zhang, J. Liu, A. Moores, S. Ghoshal, Transformation of 6:2 fluorotelomer sulfonate by cobalt(II)-activated peroxymonosulfate, *Environ. Sci. Technol.* 54 (2020) 4631–4640.
- [89] S. Wang, J. Wu, X. Lu, W. Xu, Q. Gong, J. Ding, B. Dan, P. Xie, Removal of acetaminophen in the Fe<sup>2+</sup>/persulfate system: Kinetic model and degradation pathways, *Chem. Eng. J.* 358 (2019) 1091–1100.
- [90] R. Zhou, J. Zhao, N. Shen, T. Ma, Y. Su, H. Ren, Efficient degradation of 2,4-dichlorophenol in aqueous solution by peroxymonosulfate activated with magnetic



- spinel  $\text{FeCo}_2\text{O}_4$  nanoparticles, *Chemosphere* 197 (2018) 670–679.
- [91] C. Gong, F. Chen, Q. Yang, K. Luo, F. Yao, S. Wang, X. Wang, J. Wu, X. Li, D. Wang, G. Zeng, Heterogeneous activation of peroxymonosulfate by Fe-Co layered doubled hydroxide for efficient catalytic degradation of Rhodamine B, *Chem. Eng. J.* 321 (2017) 222–232.
- [92] S. Hou, L. Ling, D.D. Dionysiou, Y. Wang, J. Huang, K. Guo, X. Li, J. Fang, Chlorate formation mechanism in the presence of sulfate radical, chloride, bromide and natural organic matter, *Environ. Sci. Technol.* 52 (2018) 6317–6325.
- [93] G. Sheng, J. Hu, A. Alsaedi, W. Shammakh, S. Monaque, F. Ye, H. Li, Y. Huang, A.S. Alshomrani, T. Hayat, B. Ahmad, Interaction of uranium(VI) with titanate nanotubes by macroscopic and spectroscopic investigation, *J. Mol. Liq.* 212 (2015) 563–568.
- [94] T. Azuma, N. Arima, A. Tsukada, S. Hirami, R. Matsuoka, R. Moriwake, H. Ishiuchi, T. Inoyama, Y. Teranishi, M. Yamaoka, Y. Mino, T. Hayashi, Y. Fujita, M. Masada, Detection of pharmaceuticals and phytochemicals together with their metabolites in hospital effluents in Japan, and their contribution to sewage treatment plant influents, *Sci. Total Environ.* 548–549 (2016) 189–197.
- [95] O.M. Rodríguez-Narvaez, R.D. Rajapaksha, M.I. Ranasinghe, X. Bai, J.M. Peralta-Hernández, E.R. Bandala, Peroxymonosulfate decomposition by homogeneous and heterogeneous Co: Kinetics and application for the degradation of acetaminophen, *J. Environ. Sci.* 93 (2020) 30–40.
- [96] F. Fanaei, G. Moussavi, V. Srivastava, M. Sillanpää, The enhanced catalytic potential of sulfur-doped MgO (S-MgO) nanoparticles in activation of peroxysulfates for advanced oxidation of acetaminophen, *Chem. Eng. J.* 371 (2019) 404–413.
- [97] H. Ji, P. Du, D. Zhao, S. Li, F. Sun, E.C. Duin, W. Liu, 2D/1D graphitic carbon nitride/titanate nanotubes heterostructure for efficient photocatalysis of sulfamethazine under solar light: Catalytic “hot spots” at the rutile–anatase–titanate interfaces, *Appl. Catal. B: Environ.* 263 (2020) 118357.
- [98] W. Liu, Y. Li, F. Liu, W. Jiang, D. Zhang, J. Liang, Visible-light-driven photocatalytic degradation of diclofenac by carbon quantum dots modified porous  $\text{g-C}_3\text{N}_4$ : Mechanisms, degradation pathway and DFT calculation, *Water Res.* 151 (2019) 8–19.
- [99] Z. Cai, X. Hao, X. Sun, P. Du, W. Liu, J. Fu, Highly active  $\text{WO}_3/\text{anatase-SiO}_2$  aerogel for solar-light-driven phenanthrene degradation: Mechanism insight and toxicity assessment, *Water Res.* 162 (2019) 369–382.